# Asymmetric Rainband Processes Leading to Secondary Eyewall Formation in a Model Simulation of Hurricane Matthew (2016)

CHAU-LAM YU, ab ANTHONY C. DIDLAKE JR., FUQING ZHANG, A.D. ROBERT G. NYSTROMAD

Department of Meteorology and Atmospheric Science, The Pennsylvania State University, University Park, Pennsylvania
 Center for Advanced Data Assimilation and Predictability Techniques, The Pennsylvania State University,
 University Park, Pennsylvania

(Manuscript received 28 February 2020, in final form 29 September 2020)

ABSTRACT: The dynamics of an asymmetric rainband complex leading into secondary eyewall formation (SEF) are examined in a simulation of Hurricane Matthew (2016), with particular focus on the tangential wind field evolution. Prior to SEF, the storm experiences an axisymmetric broadening of the tangential wind field as a stationary rainband complex in the downshear quadrants intensifies. The axisymmetric acceleration pattern that causes this broadening is an inward-descending structure of positive acceleration nearly 100 km wide in radial extent and maximizes in the low levels near 50 km radius. Vertical advection from convective updrafts in the downshear-right quadrant largely contributes to the low-level acceleration maximum, while the broader inward-descending pattern is due to horizontal advection within stratiform precipitation in the downshear-left quadrant. This broad slantwise pattern of positive acceleration is due to a mesoscale descending inflow (MDI) that is driven by midlevel cooling within the stratiform regions and draws absolute angular momentum inward. The MDI is further revealed by examining the irrotational component of the radial velocity, which shows the MDI extending downwind into the upshear-left quadrant. Here, the MDI connects with the boundary layer, where new convective updrafts are triggered along its inner edge; these new upshear-left updrafts are found to be important to the subsequent axisymmetrization of the low-level tangential wind maximum within the incipient secondary eyewall.

KEYWORDS: Rainbands; Tropical cyclones; Data assimilation; Numerical analysis/modeling

#### 1. Introduction

Secondary eyewall formation (SEF) in tropical cyclones (TCs) is an inner-core process that initiates an eyewall replacement cycle (ERC), which can cause significant intensity and structural changes of the storm, such as a broader wind field and a larger eye (Willoughby et al. 1982; Black and Willoughby 1992). Such changes lead to an increased risk for wind damage and storm surge flooding when making landfall. Although frequently observed, particularly in major TCs (Hawkins et al. 2006), SEF is poorly forecasted and not yet fully understood, making it a prime focus of many studies in recent years (e.g., Kossin and Sitkowski 2009; Kuo et al. 2009; Fang and Zhang 2012; Abarca and Montgomery 2013; Zhang et al. 2017; Dai et al. 2017; Wang et al. 2019).

Several theories have been proposed to explain the onset of SEF, but so far there has been no clear consensus on the initiating mechanism. Montgomery and Kallenbach (1997) hypothesized SEF as the consequence of outward-propagating vortex–Rossby waves (VRWs) being stagnated at a critical radius. Other studies indicate, however, that the potential vorticity (PV) anomalies near the secondary eyewall radius are either generated locally or sourced from spiral rainbands at larger radii, instead of from the outward-propagating VRWs (Qiu et al. 2010; Judt and Chen 2010). Additionally, the hypotheses of rapid filamentation (Rozoff et al. 2006) and

Corresponding author: Chau-Lam Yu, cuy89@psu.edu

beta-skirt axisymmetrization (Terwey and Montgomery 2008) discuss how asymmetric flow in the vicinity of a large background vorticity gradient is constrained in a way that PV anomalies and eddy kinetic energy can be converted into the azimuthal mean.

One key aspect of the aforementioned eddy–mean-flow processes is the preceding change in the background wind and vorticity fields. Prior to SEF, an axisymmetric broadening of the outer tangential wind field is frequently identified in both observations (Sitkowski et al. 2011, 2012; Didlake and Houze 2013; Bell et al. 2012; Wunsch and Didlake 2018; Martinez et al. 2019) and modeling studies (Rozoff et al. 2006, 2012; Fang and Zhang 2012; Sun et al. 2013; Tang et al. 2017; Wang et al. 2016, 2019). While it is generally agreed that the wind field broadening is a precursor of SEF (Wang 2009; Moon and Nolan 2010; Rozoff et al. 2012; Zhu and Zhu 2014), there is currently no conclusive evidence about whether this broadening is the cause or the result of the ongoing SEF.

Besides the dynamical processes in the free troposphere, many studies have highlighted the role of boundary layer processes during SEF (Kepert 2013; Wu et al. 2012; Huang et al. 2012; Abarca and Montgomery 2013; Zhang et al. 2017). Huang et al. (2012) proposed a progressive boundary layer control pathway, in which the unbalanced supergradient force decelerates the boundary layer inflow and forces enhanced boundary layer convergence. Contrarily, using a steady-state hurricane boundary layer model (Kepert and Wang 2001), Kepert (2013) demonstrated that in the steady-state limit, the boundary layer updraft (that leads to secondary eyewall convection) and the accompanying supergradient force are linked to the vorticity gradient at the boundary layer top. For both

c Deceased.

hypotheses, the boundary layer is critical for strengthening convective updrafts that accelerate the axisymmetric tangential wind and form the secondary eyewall low-level wind maximum.

A number of SEF theories describe axisymmetric processes that require some preexisting axisymmetric vorticity anomaly outside of the primary eyewall to initiate the coupling between the troposphere and boundary layer (Terwey and Montgomery 2008; Rozoff et al. 2012; Kepert 2013; Zhang et al. 2017, etc.). Such an axisymmetric vorticity anomaly is likely sourced by rainband convection, which comprises initially asymmetric features with their own distinct asymmetric organization and processes occurring across different length scales. Under the influence of environmental wind shear, TC rainbands tend to form a quasi-stationary, organized system, termed the stationary band complex (SBC; Willoughby et al. 1984). Typically, the SBC is most prominent in the downshear half of the storm (Hence and Houze 2012), where nascent convective cells are initiated and organized into banded structures in the right-ofshear quadrants (e.g., Corbosiero and Molinari 2002, 2003), and then slowly collapse into widespread stratiform precipitation in the left-of-shear quadrants (Didlake and Houze 2013; Riemer 2016).

Owing to its extensive spatial coverage near the storm inner core, the stratiform sector of the SBC may have a critical role in SEF processes, despite having less vigorous vertical exchanges than its upwind counterpart. A number of studies, indeed, highlight the importance of stratiform rainband processes during SEF (Qiu and Tan 2013; Fang and Zhang 2012; Didlake and Houze 2013; Dai et al. 2017; Zhang et al. 2017; Didlake et al. 2018). Didlake and Houze (2013) found a mesoscale descending inflow (MDI) in the stratiform rainband complex of Hurricane Rita, which extended from the mid- to upper troposphere into the boundary layer. Didlake et al. (2018) later found a similar MDI in Hurricane Earl (2010), which had a robust vertical updraft on its inward side that contributed to the subsequent SEF. Using idealized simulations with imposed rainband forcing, Yu and Didlake (2019) demonstrated that this MDI brings negatively buoyant air toward the surface and forces persistent low-level updrafts along the inner edge of the surface cold pool. This finding also agrees well with the earlier idealized study by Qiu and Tan (2013), who demonstrated that diabatic cooling induced by an asymmetric descending inflow was able to support the development of a new convective updraft at its inner edge, contributing to the subsequent development of a secondary eyewall. Several modeling studies later also showed that latent cooling in stratiform rainband precipitation is critical for enhancing outer core convection (Cai and Tang 2019), and ultimately increasing the likelihood of secondary eyewall formation (Li et al. 2014; Zhu et al. 2015; Tang et al. 2017; Tyner et al. 2018; Chen 2018; Chen et al. 2018).

In this study, we extend upon previous research to investigate the processes of the asymmetric rainband complex in a TC leading into the formation of a secondary eyewall. Our investigation utilizes a high-resolution, convection-permitting simulation of Hurricane Matthew (2016) that is initialized using an ensemble-Kalman filter data assimilation system, incorporating both conventional and airborne radar observations. Prior

to the SEF period, the simulated storm develops a shearaligned stationary rainband complex that contributes dynamically to the subsequent formation of a secondary eyewall. This study will primarily focus on the asymmetric convective and stratiform processes that contribute to the local and axisymmetric tangential wind acceleration of the evolving storm.

This paper is organized as follows. Section 2 gives an overview of Hurricane Matthew (2016) and introduces the model settings and initial conditions. Section 3 describes the evolution of the secondary eyewall formation in the Matthew simulation. Section 4 examines the wind field acceleration from an axisymmetric perspective. The along band structure of SBC is examined in section 5, followed by a detailed quadrant-averaged tangential wind budget analysis in section 6. Section 7 examines the evolution of the MDI. Section 8 summarizes and concludes the findings.

#### 2. Model and data

This study examines a high-resolution full-physics simulation of Hurricane Matthew (2016) during its time of peak intensity (maximum winds of 67 m s<sup>-1</sup> and minimum pressure of 940 hPa) located in the Caribbean Sea. The simulation uses WRFv3.5.1 (Skamarock et al. 2008) and consists of four twoway nested domains (the three innermost domains being vortex following) with horizontal grid spacings of 27, 9, 3, and 1 km, respectively. Domains are configured identical to that described in Zhang and Weng (2015) with the exception of the innermost domain (499 × 499 grid points), which has been added for the forecast to better resolve the TC inner core. The model physics are also identical to that in Zhang and Weng (2015), which include the WSM6 microphysics scheme (Hong et al. 2004), the YSU boundary layer scheme (Noh et al. 2003), and the Grell-Devenyi ensemble cumulus scheme (Grell and Freitas 2014; only in the outermost domain).

This study focuses on the SEF event of Matthew near 0000 UTC 3 October. The model simulation is initialized from an EnKF analysis mean at 0000 UTC 2 October 2016, which is 24 h before the SEF event. The EnKF cycling data assimilation is performed identically to previous studies using the Pennsylvania State University WRF EnKF system (e.g., Munsell and Zhang 2014; Weng and Zhang 2016; Nystrom et al. 2018) and begun at 1800 UTC 25 September 2016. Synthetic hurricane position and intensity observations, all available conventional observations, and airborne Doppler radar super observations (Gamache et al. 1995; Weng and Zhang 2012) and dropsonde observations are assimilated at a 3-h cycling frequency. To better resolve the observed small eye of Matthew (radius of maximum wind of about 10 km; Stewart 2017), the innermost domain of 1-km horizontal grid spacing is added for the purposes of this study, as in Nystrom and Zhang (2019). The boundary conditions for this simulation are from the GFS forecast initialized from 0000 UTC 2 October. All the analyses in this study are performed using model output with 5-min interval.

As shown in Figs. 1a and 1b, the simulated storm matched the real storm well, having a similar track during our period of focus. The simulated storm has a similar minimum sea level

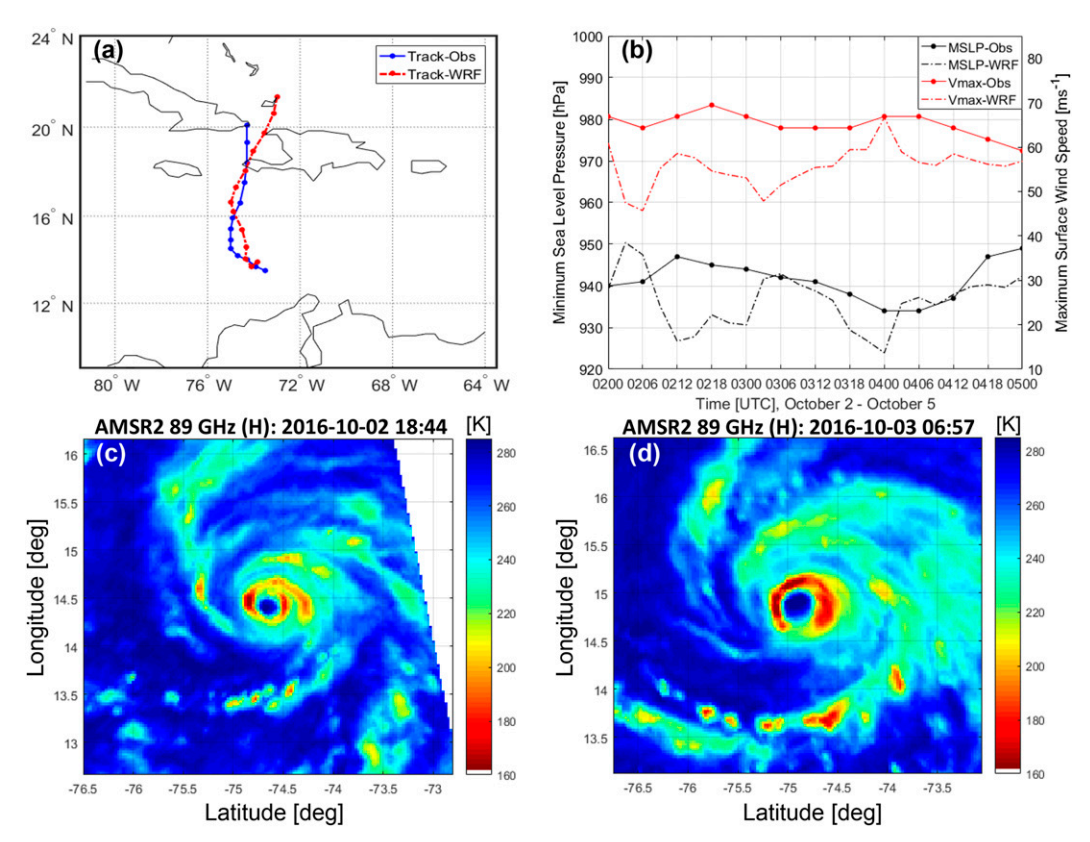


FIG. 1. (a) Observed and simulated tracks during the 72-h simulation period from 0000 UTC 2 Oct to 0000 UTC 5 Oct 2016. The observed track comes from the National Hurricane Center best track data. (b) Observed and simulated minimum sea level pressure (MSLP; black) and maximum surface wind (Vmax; red). Observed intensities are dotted solid lines, and simulated intensities are dashed lines. (c),(d) Observed 89 GHz brightness temperatures of the Advanced Microwave Scanning Radiometer 2 (AMSR2) before and after the simulated SEF.

pressure but slightly weaker maximum winds than the real storm. Figures 1c and 1d show the observed microwave brightness temperatures of Matthew before and after the times of our simulated ERC. While conclusive observations of a secondary eyewall and ERC are lacking, the satellite images show an appreciable increase in the eye diameter from about 9 km near 1900 UTC 2 October to 17 km near 0700 UTC 3 October. A comparable eye size increase is well captured in the simulated storm near the same time period (Fig. 2), which undergoes an ERC near 0100 UTC 3 October. Despite any differences with observations, a detailed analysis of the simulated storm will provide useful insight into SEF mechanisms.

#### 3. Overview of SEF in the Matthew simulation

Figure 2 shows the azimuthally averaged vertical motion at z=1.5 km and tangential wind at z=2.86 km for the first 36-h simulation period. After 7h of the spinup period, the storm stabilizes at an intensity of  $\sim 110$  kts  $(1 \text{ kt} \approx 0.51 \text{ m s}^{-1})$ , with a radius of maximum wind of  $\sim 10$  km. The storm maintains its intensity until hour 16, after which clear axisymmetric projection of an outer updraft (Fig. 2a) and sudden kink in the azimuthal mean tangential wind emerge near 60 km radius

(Fig. 2b). These signals mark the beginning of SEF, and they steadily contract inward. We define the secondary eyewall as being formed once shear-relative quadrant-averaged profiles of vertical velocity indicate that secondary peak of updrafts emerges in all quadrants. In our simulation, this occurs first at hour 22. This definition of a formed secondary eyewall allows us to further distinguish the axisymmetric updraft signal of a well-established secondary eyewall from the azimuthal mean projection of the updraft of the rainband complex. However, in an axisymmetric mean perspective, we can see from Fig. 2a that these two features are indeed dynamically linked to each other as they form a clear continuous inward-contracting signal. Based on this definition, we define the time period from hour 15 to 22 as the SEF period, while the sequence after hour 22 as the ERC period (hour 23 to 25). During the SEF period (hour 15 to 22), the 850-200 hPa wind shear is stable and maintained at a moderate value of about 5 m s<sup>-1</sup>. The temporally averaged environmental wind structure (from hour 15 to 25) and 850-200 hPa wind shear is shown in Fig. 2c, together with the evolutions of the shear direction and magnitude in Fig. 2d. The 850-200 hPa wind shear is computed as the annulus mean wind field difference within the 200 and 500 km radial range between the two pressure levels using the 9km model output. After hour 22, the inner eyewall updrafts weaken and the primary

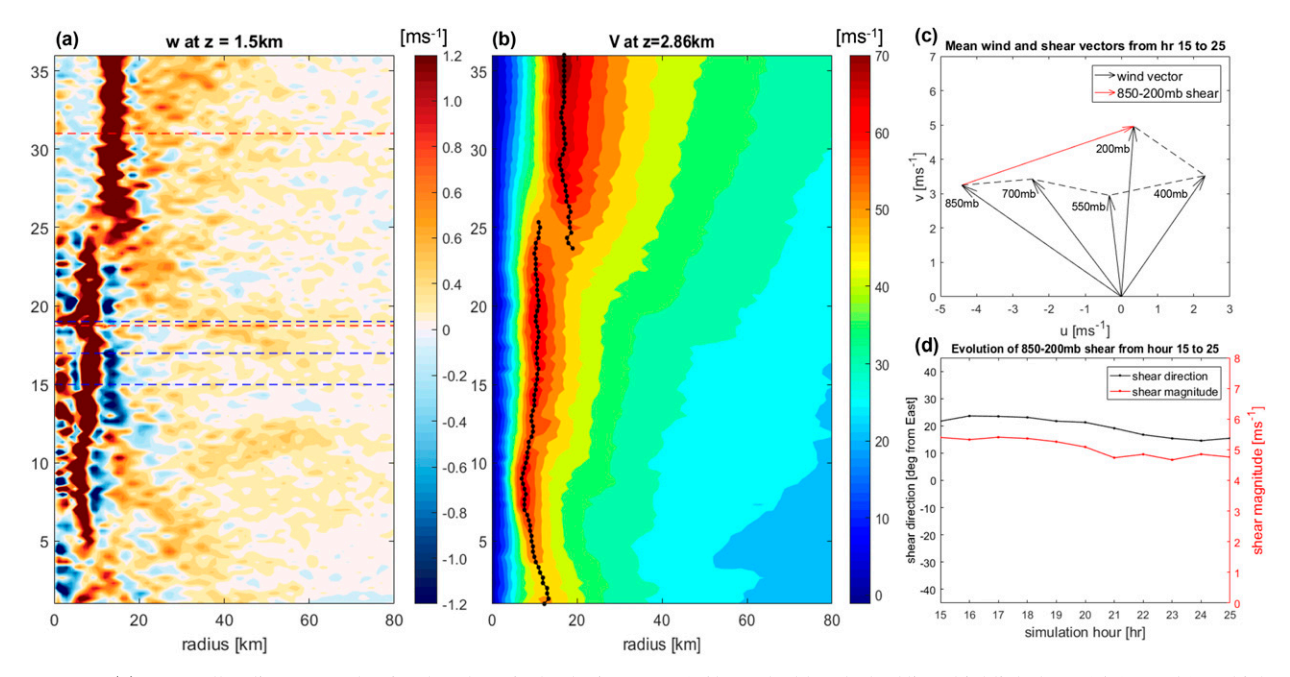


FIG. 2. (a) Hovmöller diagram of the simulated vertical velocity at z = 1.5 km. The blue dashed lines highlight hour 15, 17, and 19, which correspond to the hours of the wind acceleration fields shown in Fig. 5. The red dashed lines indicate the times of the observed AMSR2 brightness temperature shown in Figs. 1c and 1d. (b) As in (a), but for tangential velocity at z = 2.86 km. Black dotted lines indicate radius of maximum wind of the primary and secondary eyewalls. (c) Hodograph of environmental wind at 850, 700, 550, 400, and 200 mb (black) and 850–200 mb shear (red), temporally averaged over hours 15 to 25. (d) Time evolution of the 850–200 mb shear direction (black) and magnitude (red) from hours 15 to 25.

eyewall is subsequently replaced by the newer eyewall at hour 25, which continues at a larger radius ( $\sim$ 20 km).

To see the storm structure leading to the SEF event more clearly, Figs. 3 and 4 show plan views and axisymmetric cross sections at selected hours during the SEF period. Near hour 15, a stationary band complex (SBC) develops in the downshear quadrants, which exhibits strengthening maxima of reflectivity and vertical velocity (Figs. 3b,c,h,i). During hours 15 to 19, the azimuthal mean projections of the vertical velocity and diabatic heating of the SBC not only display an increase in magnitude and areal coverage, but also a clear inward contraction from about 60 to 30 km radius, as shown in Figs. 4a-c,g-i and 2a. Looking at the plan view, as in Figs. 3gi, we see that rainband updrafts show clear downwind shift from the downshear-right (DR) quadrant near 60 km radius at hour 15 toward the downshear-left (DL) quadrant near 40 km radius at hour 19. This confirmed that the inwardcontracting azimuthal updraft signal largely comes from the strengthening mesoscale updrafts associated with the downwind development of the intensifying SBC. Along with this enhancing diabatic heating, both the tangential wind and the midlevel inflow strengthen progressively, as in seen Figs. 4c and 4i. Consistent with previous studies (Zhang et al. 2017; Wang et al. 2019), the diabatic heating and updrafts of the SBC largely maximize at the mid- to upper level above 4km during hour 15 to 19. These maxima then descend toward the low levels and become connected to the boundary layer after hour 21 (Figs. 4d-f,j-l). As shown in Fig. 2a, this inward contraction gives rise to the typical evolution of SEF,

demonstrating that the secondary eyewall indeed stems from this intensifying SBC.

Near hour 21, the rainband starts to axisymmetrize when the updrafts at the downwind sector of SBC continuously propagate and wrap around the storm (Figs. 3d,e,j,k). During this axisymmetrization period, the azimuthal mean updraft and diabatic heating interact and seemingly connect with the boundary layer (Figs. 4d–f,j–l). Figure 3k also clearly demonstrates that secondary peak of updraft forms a clear circular ring at hour 22, marking the establishment of the secondary eyewall. In the subsequent hours, this axisymmetric signal further strengths (Figs. 3f,l) and replaces the primary eyewall near hour 25.

## 4. Storm-scale changes in tangential velocity and angular momentum

### a. Tangential velocity analysis

Prior to the simulated SEF, an organized tangential wind broadening is found to be associated with the intensifying asymmetric rainband complex during hours 15–20. Figure 5 shows the azimuthally averaged cross section and vertically averaged plan view (between  $z=2-6\,\mathrm{km}$ ) of the stormfollowing tangential velocity changes at the selected SEF hours. Early at hour 15 when the rainband starts to develop, the azimuthally averaged tangential velocity acceleration is generally weak (Fig. 5a). The strongest acceleration is located in the downshear-right quadrant outward of 40 km

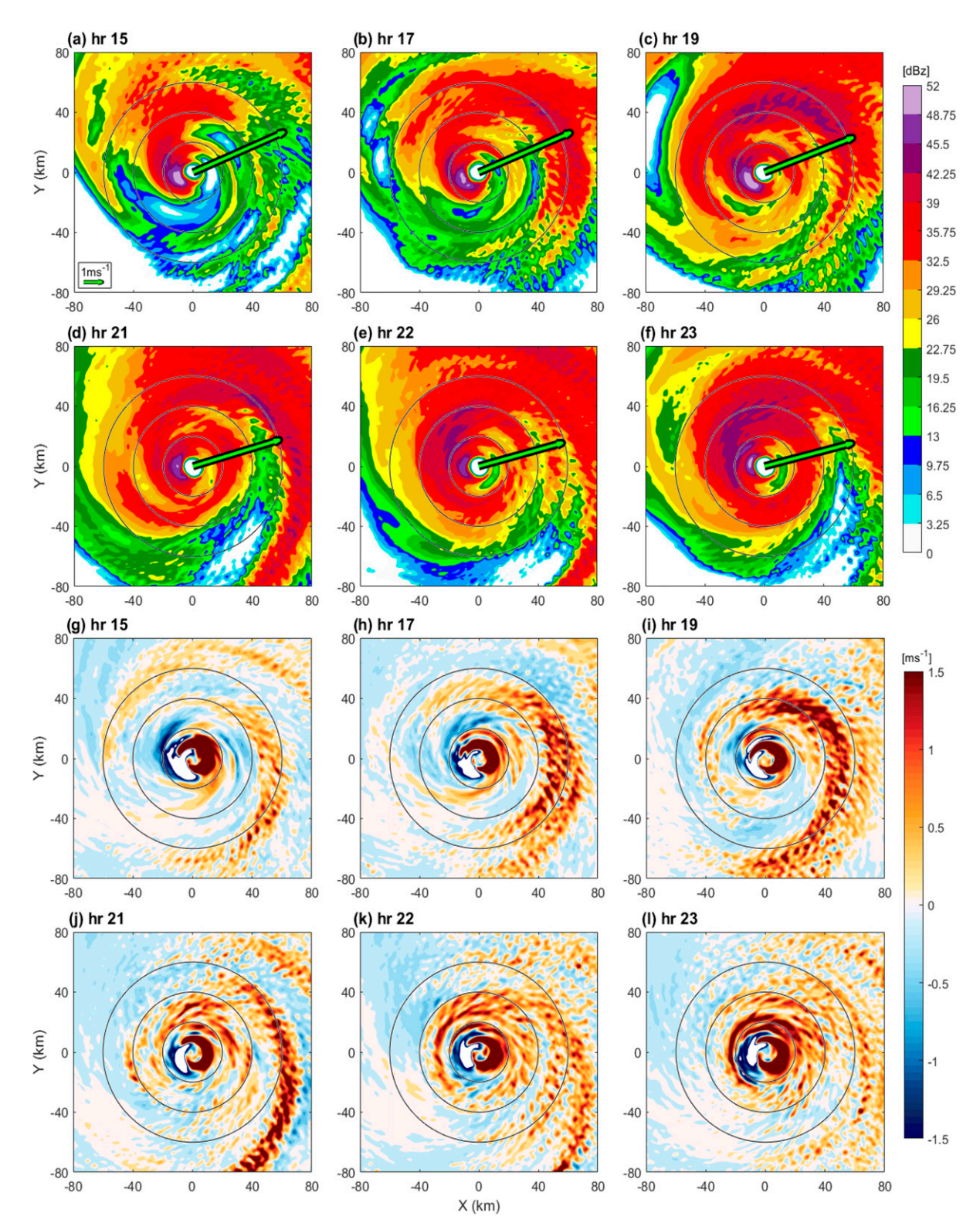


FIG. 3. Plan views of (a)–(f) reflectivity averaged between z=0.5 and 4 km and (g)–(l) vertical velocity at z=4 km at simulation hours 15, 17, 19, 21, 22, and 23. Green arrows indicate the 850–200 mb vertical wind shear vector. Black circles indicate 20, 40, and 60 km radii. All fields in subsequent figures are temporally averaged over the 1-h period of the corresponding simulation hour, unless otherwise specified.

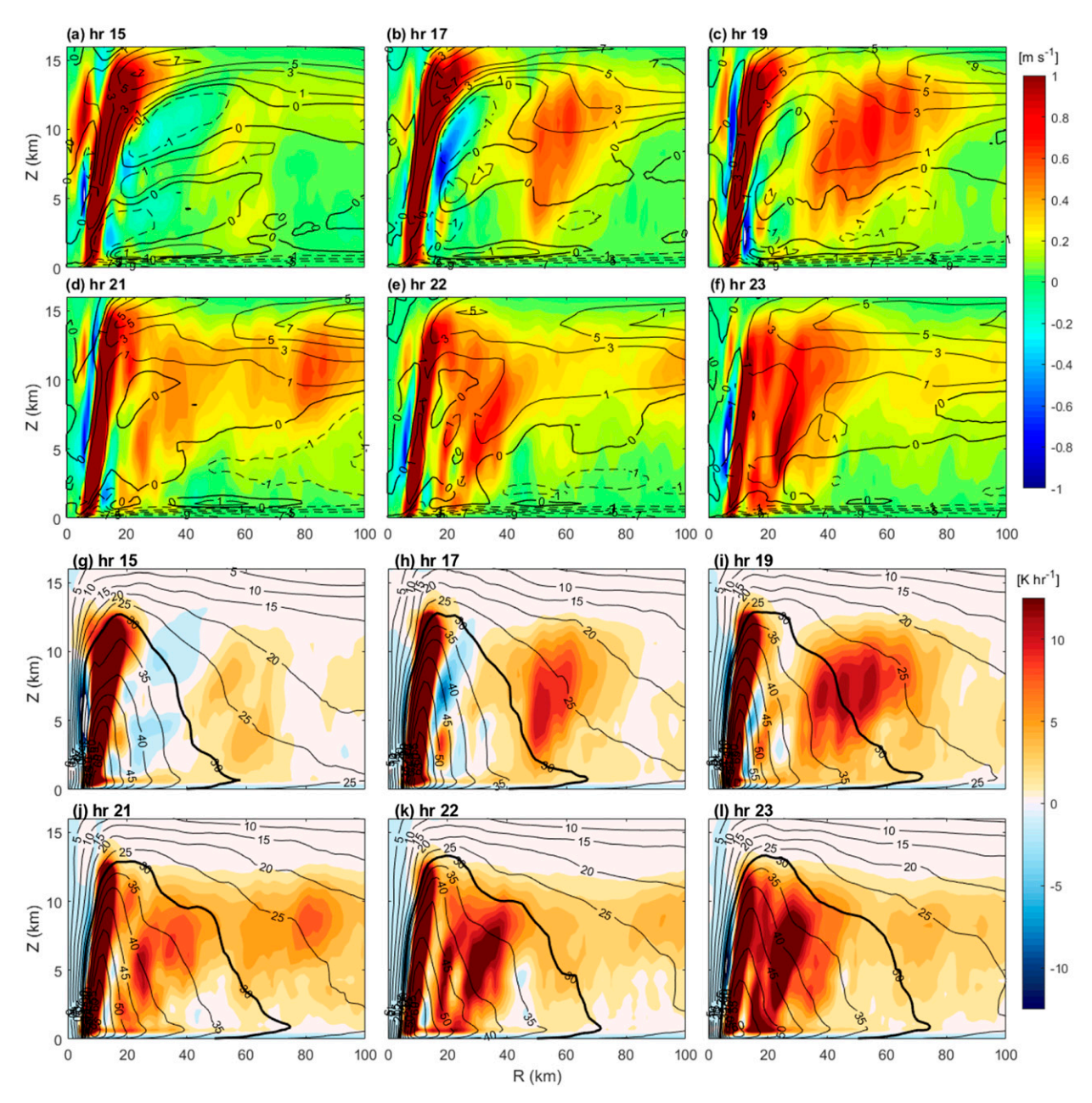


FIG. 4. (a)–(f) R–Z cross sections of azimuthally averaged vertical velocity (shading) and radial velocity (contoured in black every 2 m s<sup>-1</sup> with the zero line thickened) at selected hours of 15, 17, 19, 21, 22, and 23. (g)–(l) As in (a)–(f), but for diabatic heating (shading) and tangential wind (contoured in black every 5 m s<sup>-1</sup> with 30 m s<sup>-1</sup> line thickened).

radius, and is associated with the enhanced boundary layer inflow and vertical momentum exchange of the intensifying rainband.

After just 2 h, at hour 17, the azimuthally averaged acceleration becomes significantly more intense and broader in scale between 2 and 6 km altitude (Figs. 5b,e). The region of positive acceleration shows an inward-descending pattern from mid-to upper levels (between z = 5 and 10 km) and maximizes between r = 40 and 60 km. Looking at the plan view (Fig. 5e), once the rainband intensifies, the acceleration in both the

DL and DR quadrants become more organized and project strongly onto the azimuthal mean. Specifically, the acceleration in the DR quadrant is strong but mostly concentrated at 50–60 km radii, while the acceleration in the DL quadrant is similarly strong but noticeably more widespread. Quadrant averages of the acceleration field (not shown) indicate that the acceleration in the DL quadrant extends beyond 120 km radius. This analysis demonstrates that while the acceleration maximum near 50 km radius in Fig. 5b receives contribution from both DR and DL quadrants, the broadscale descending

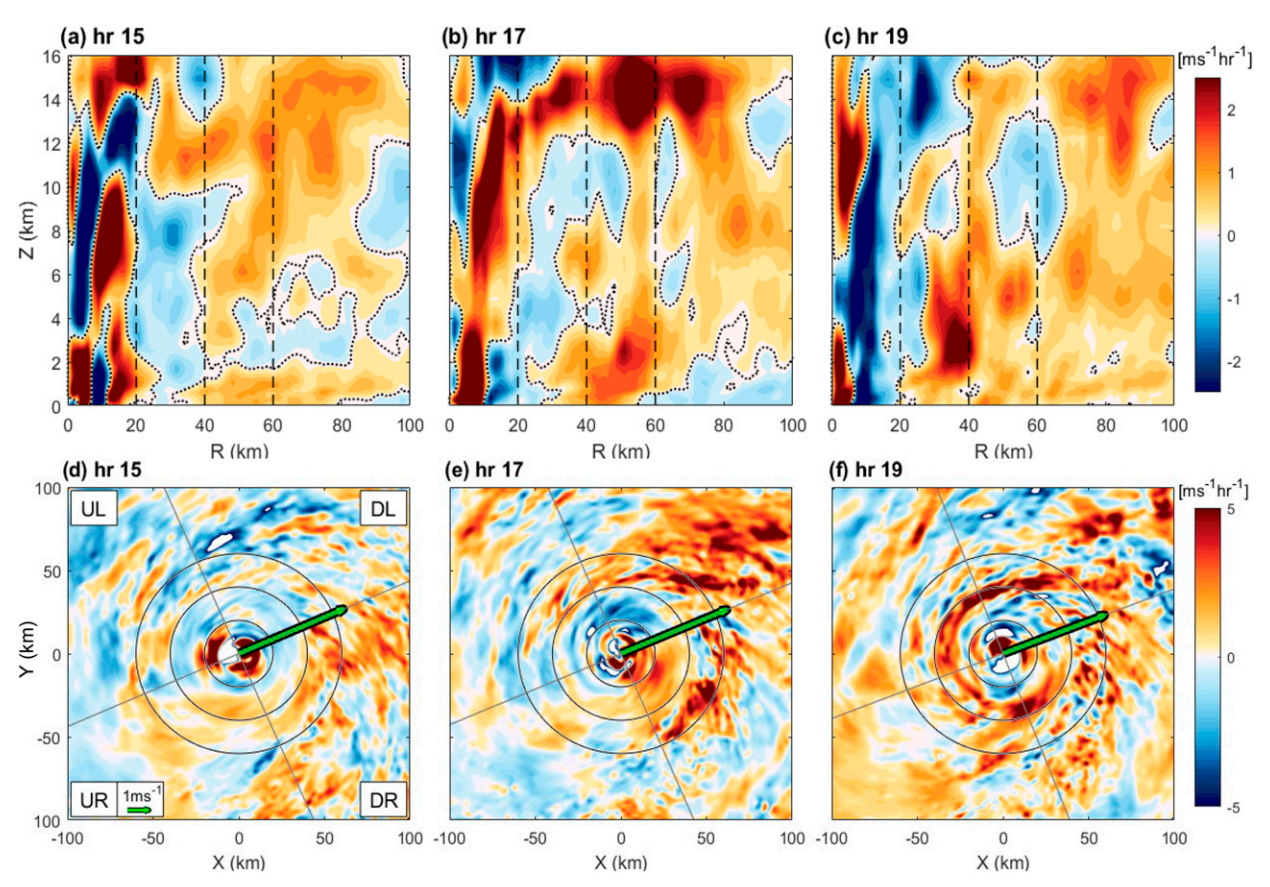


FIG. 5. (top) R–Z cross sections of azimuthally averaged tangential wind acceleration at hours (a) 15, (b) 17, and (c) 19. Zero contour is plotted in black dotted line. Vertical black dashed lines indicate 20, 40, and 60 km radii. (bottom) Plan views of hourly storm-relative tangential wind changes averaged between z = 2 and 6 km at hours (d) 15, (e) 17, and (f) 19. Green arrows indicate the 850–200 mb vertical wind shear vector, with black straight lines highlighting individual quadrants. Black circles indicate 20, 40, and 60 km radii.

pattern in the mean acceleration largely comes from the DL quadrant.

At hour 19, positive acceleration extends from the DL quadrant toward the upshear quadrants, while acceleration in the DR quadrant weakens. The resulting pattern is a more axisymmetric acceleration band that maximizes near the 30 to 40 km radii and projects strongly onto the azimuthal mean, as shown in Figs. 5c and 5f. This axisymmetric acceleration indicates that the storm wind field is becoming more axisymmetric during hour 19. Looking at the reflectivity (Fig. 3c) and updrafts (Fig. 3i) at hour 19, we see that the upshear quadrants are mostly free of strong convection but is covered with moderate reflectivity about 30–40 dBZ. As will be shown in section 5, this acceleration pattern also has a descending trend toward its downwind end. The mechanisms of the wind acceleration during hour 17 and 19 will be explored in more details in later sections.

#### b. Angular momentum budget analysis

Given the distinct patterns of positive tangential velocity acceleration at hours 17 and 19, we now focus our attention on these particular hours leading into SEF. As shown in Fig. 5e, hour 17 is the earliest hour when systematic storm-scale

tangential velocity acceleration first occurs accompanying the intensifying rainband, while at hour 19 the tangential wind field acceleration starts to extend toward the upshear quadrants and becomes more axisymmetric. To quantify the dynamical processes that contribute to the acceleration, the axisymmetric storm-relative angular momentum budget is performed for these two selected hours. The budget is calculated using

$$\frac{\partial_{c} \overline{M}_{ST}}{\partial t} = -\overline{u}_{ST} \frac{\partial \overline{M}_{ST}}{\partial r} - \overline{w} \frac{\partial \overline{M}_{ST}}{\partial z} - \overline{u}_{ST}' \frac{\partial \overline{M}_{ST}'}{\partial r} - \overline{w}' \frac{\partial \overline{M}_{ST}'}{\partial z} - \overline{u}_{ST}' \frac{\partial \overline{M}_{ST}'}{\partial r} - \overline{w}' \frac{\partial \overline{M}_{ST}'}{\partial z}$$

$$- \frac{1}{\rho} \frac{\partial p}{\partial \lambda} + r \overline{F_{\lambda}}, \qquad (1)$$

where  $\partial_c/\partial t$  denotes local time derivative that follows the storm center; the overbar denotes azimuthal average about storm center; the prime symbol denotes deviation from the azimuthal mean;  $(r, \lambda, z)$  represents storm-following cylindrical coordinate;  $u_{\rm ST}$  and  $v_{\rm ST}$  are the storm-relative radial and tangential winds;  $M_{\rm ST} = rv_{\rm ST} + (1/2)fr^2$  is the absolute angular momentum of the storm relative wind; w is vertical motion; p is pressure; p is density; and  $F_{\lambda}$  is friction along the tangential direction. The terms at the right-hand side of (1) are the mean radial and vertical advections, radial and vertical eddy momentum advections, and

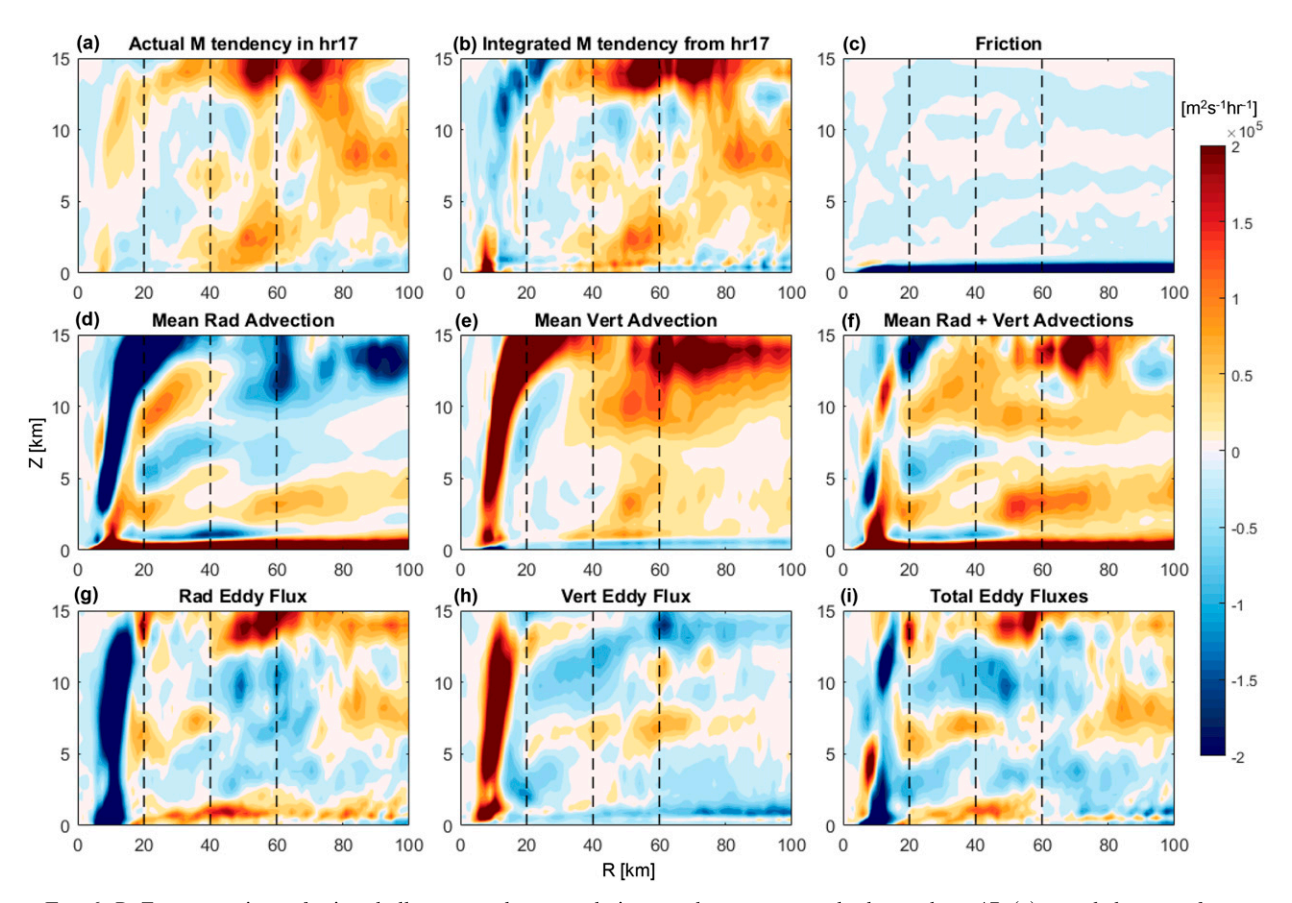


FIG. 6. *R–Z* cross sections of azimuthally averaged storm-relative angular momentum budget at hour 17: (a) actual changes of storm-relative angular momentum, (b) integrated changes of angular momentum using 5-min model output, (c) contribution from friction, (d) advection by mean radial flow, (e) advection by mean vertical velocity, (f) sum of mean-flow advection, (g) radial eddy flux, (h) vertical eddy flux, and (i) sum of eddy contributions. Vertical dashed lines indicate 20, 40, and 60 km radii.

contributions from the pressure gradient force and the boundary layer friction, respectively.

Figure 6 shows the actual and integrated hourly changes of absolute angular momentum during hour 17, and the corresponding terms at the right-hand side of Eq. (1). The baroclinic pressure gradient term is negligible and is not shown. The diagnosed  $M_{\rm ST}$  changes (Fig. 6b) are forward integrated using 5-min model output. As shown in Fig. 6a, during hour 17 the absolute angular momentum exhibits a broadscale increase between 40 and 120 km radii. This tendency displays a descending trend toward inner radii and has a local maximum at the mid- to low levels near 40 to 60 km radii, which is consistent with the tangential acceleration shown in Fig. 5b. Looking at the integrated M changes shown in Fig. 6b, it is clear that the all major tangential acceleration patterns are nicely represented.

During hour 17, the mean-flow contribution to  $M_{\rm ST}$  is largely positive throughout the midtroposphere (Fig. 6f). In contrast, the total eddy contribution (Fig. 6i) is largely negative at the same region, resulting in slight cancellation with the mean flow contribution. However, positive eddy contribution is found outside of 70 km radius above 7 km altitude, as well as near 40 km radius within the boundary layer. Further breaking down the mean flow advection term, both mean radial (Fig. 6d)

and vertical advection (Fig. 6e) are important to the total mean flow contribution at hour 17. Specifically, the mean radial advection has a broad positive contribution that covers from 50 to 100 km radius between 3 and 5 km altitude. On the other hand, the vertical advection term has positive contribution that concentrates near 50 km radius. Recall from Fig. 5a that the DR quadrant has a concentrated positive acceleration centered between 50 and 60 km radii, whereas the acceleration in the DL quadrant is similarly strong but covers a much wider radial range. Figures 6d and 6e suggest that the different acceleration patterns in these two quadrants may be due to two distinct modes of mean flow accelerations. This possibility will be further examined in more detail in section 6.

Moving on to hour 19 when the wind field starts to undergo axisymmetrization, Fig. 7a shows that the increase in the angular momentum is noticeably more extensive than in hour 17. The integrated  $M_{\rm ST}$  changes shown in Fig. 7b are again in good agreement with the actual changes. Looking into individual terms, the total mean flow contribution (Fig. 7f) is almost uniformly and strongly positive outside  $r=30\,{\rm km}$  radius below 7 km altitude, and is the dominant component of the positive total tendency in the midtroposphere. Between 50 and 80 km radii, this mean flow contribution has a local maximum

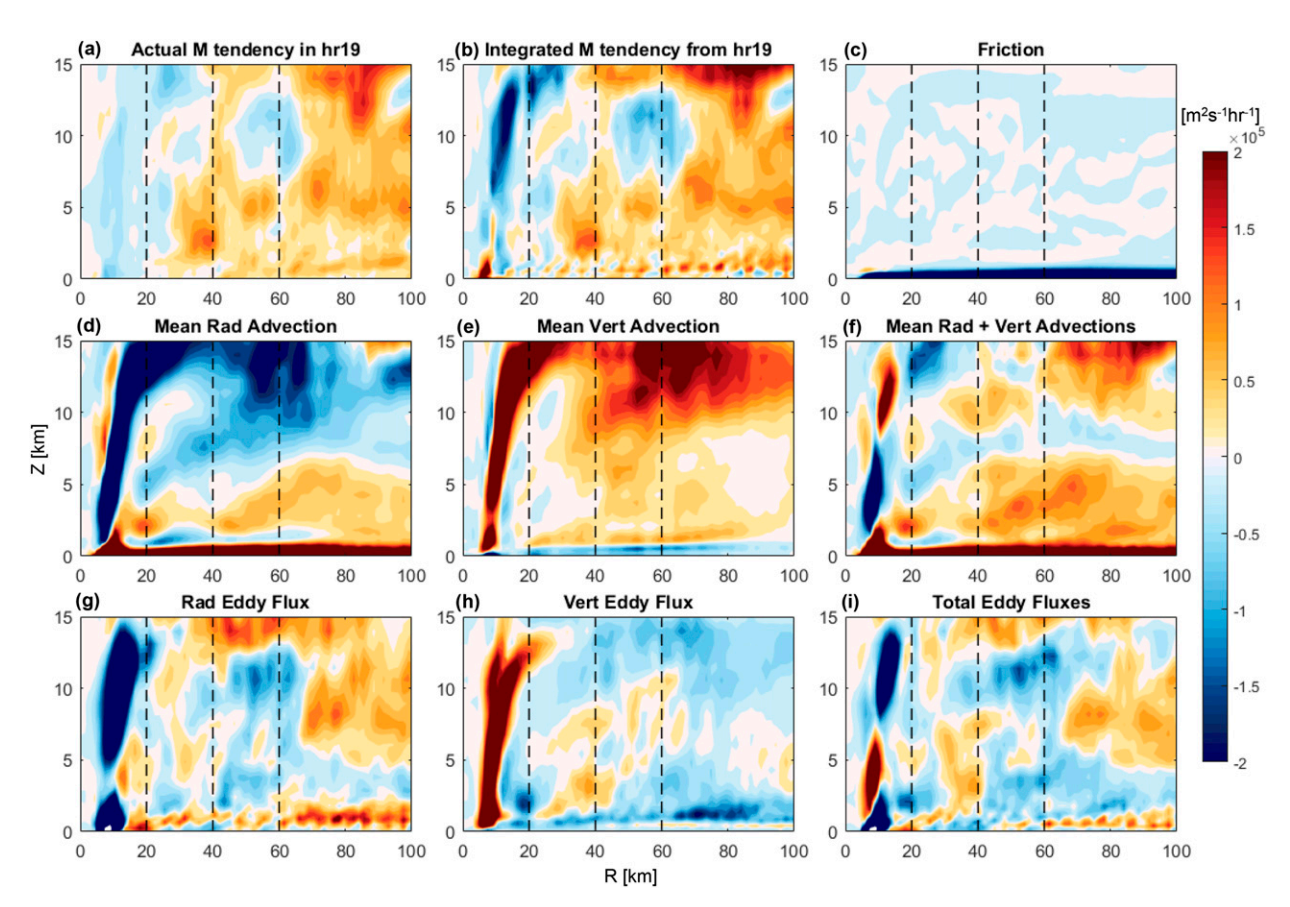


FIG. 7. As in Fig. 6, but for hour 19.

descending from 6 km altitude toward low levels at inner radii. This pattern largely is reflected in the mean radial advection (Fig. 7d), which shares the same descending structure. The mean vertical advection term (Fig. 7e) is also positive, but is overall weaker near this region. At hour 19, we note that the regions with positive mean radial advection cover a larger radial range compared to that in hour 17, which is due to an increase of the midlevel mean radial inflow (Fig. 4c).

During hour 19, eddies also have positive contributions outside 70 km radii above 5 km altitude and between 30 and 40 km radii at midlevels. Specifically, the positive eddy contribution near 30–40 km radii comes largely from the vertical eddy flux term. This region sits at the inner edge of positive mean flow contribution, and is seemingly connected to the boundary layer. While this positive eddy contribution is somewhat weak, it actually is an important contribution to the positive tendency in the total integrated tendency within 40 km radius. Consistent with Wang et al. (2019), this suggests that the boundary layer eddy processes and the associated updrafts are important to the axisymmetrization during hour 19.

## 5. Asymmetric along-band structure

To further understand the three-dimensional structure of the rainband complex during the SEF period, we examine the variations in kinematic variables along the spiral rainband in a fashion similar to that in Wang et al. (2019). Using cubic splines with natural boundary conditions (Vetterling et al. 1992), we define spirals using seven subjectively determined anchor points that pass through the rainband-induced convergence maxima shown by the vertically averaged (2–5 km) horizontal divergence fields for hours 17 and 19 (Fig. 8). The azimuthal direction of the third anchor point always aligns with the wind shear vector, while the azimuthal coordinates of the remaining six anchor points are defined accordingly with a 30° spacing. The resulting spirals span an azimuthal range of 180° divided into six sectors, labeled A–F.

Figures 9a and 9b show the along-band cross section of the rainband at hour 17. During hour 17, the rainband is steadily intensifying, with growing convective cells in the downshear quadrants. This is reflected in the vertical velocity field (Fig. 9a), which has more intense vertical motions in sectors A and B of the DR quadrant. Traveling into the DL quadrant, the updraft magnitudes decrease significantly, and a weak downdraft develops below 2.5 km altitude in sectors D–F. The diabatic heating (Fig. 9b) displays the same overall pattern. The magnitudes and pattern of the vertical velocity and heating indicate that the rainband in the DL quadrant is more stratiform in nature, consistent with previous observational (Hence and Houze 2012; Didlake and Houze 2013) and modeling studies (Wang et al. 2019).

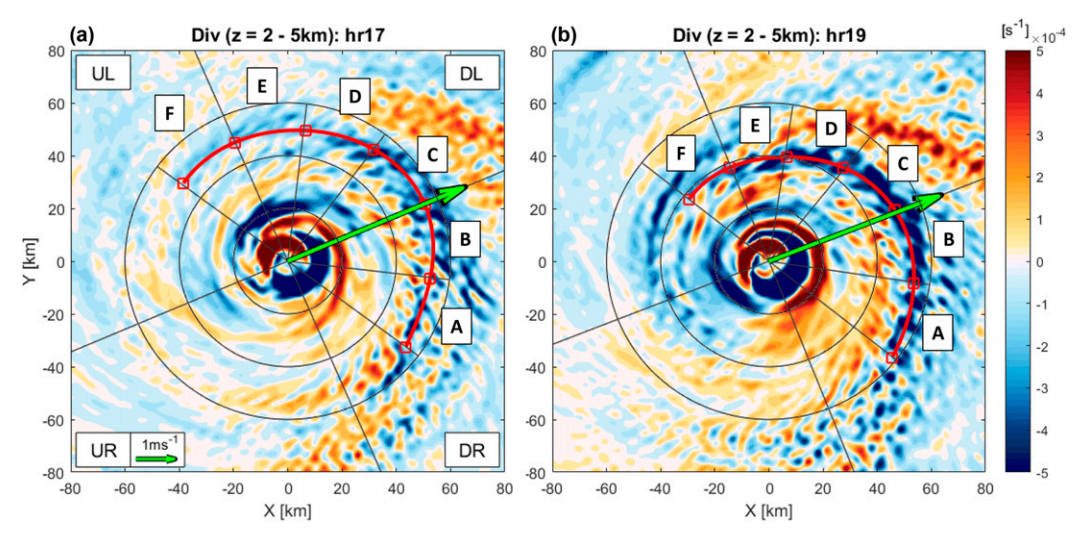


FIG. 8. Plan views of vertically averaged horizontal divergence between z=2 and 5 km for hours (a) 17 and (b) 19. Green arrow indicates the 850–200 mb shear vector. Red squares are the anchor points, with the third one aligning with the shear vector. Red spiral line is defined by the anchor points using cubic spline. Long solid black lines define the quadrants; short solid black lines define individual sectors labeled A–F. The three circles indicate 20, 40, and 60 km radii.

The tangential wind acceleration also displays significant structural changes along the rainband. In the DR quadrant (sectors A–B), owing to the more intense vertical motions which advect strong tangential winds to the upper levels, the tangential wind acceleration above  $z=10\,\mathrm{km}$  is strongly positive, as highlighted by the contours in Fig. 9a. Traveling

downwind into sectors C–F, the positive acceleration region descends toward 3 km altitude. Because of this descending acceleration field, the associated asymmetric tangential wind  $(v_a)$  also shares a similar structure. Here, the asymmetric tangential wind is computed by first removing the environmental component  $(\mathbf{v}_{\text{env}})$  from the storm-relative wind  $(\mathbf{v}_{\text{ST}})$ , and then

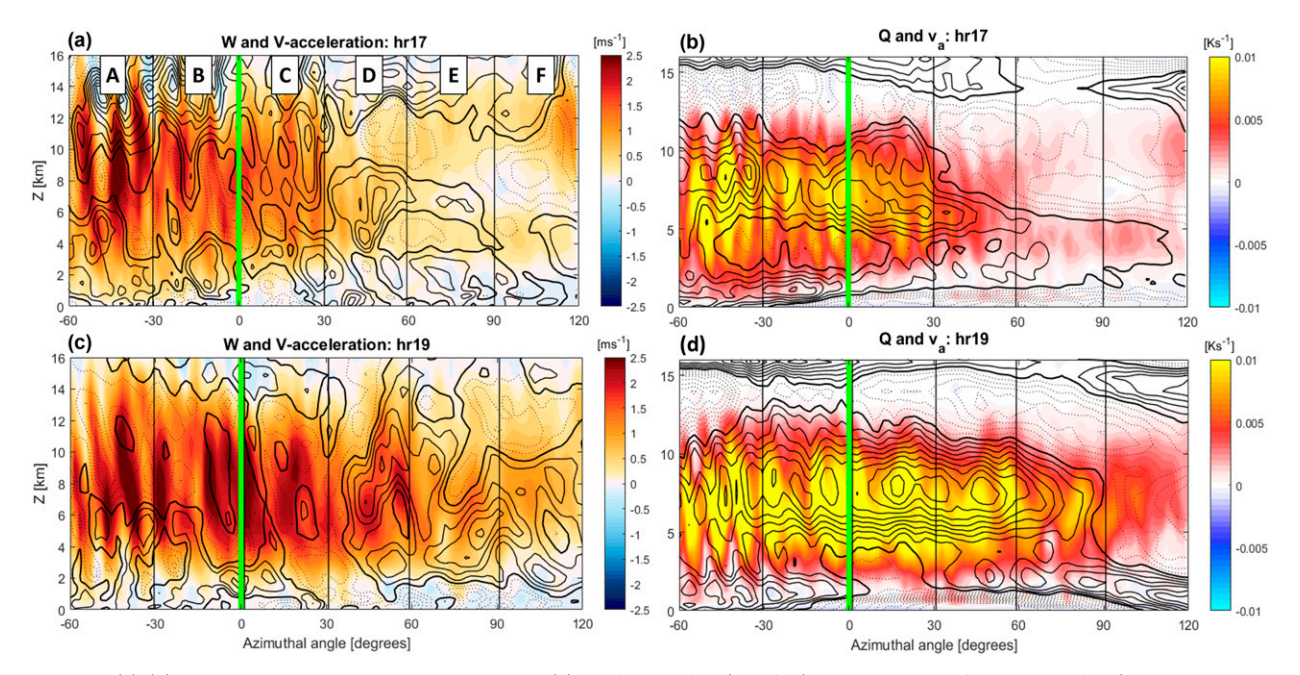


FIG. 9. (a),(b) Along-band cross sections of hour 17 for (a) vertical motion (shading) and tangential wind acceleration (contoured every  $2 \text{ m s}^{-1} \text{ h}^{-1}$ , negative contours are dashed, smallest positive contour of  $1 \text{ m s}^{-1} \text{ h}^{-1}$  is thickened), and (b) the diabatic heating (shading) and asymmetric tangential wind  $v_a$  (contoured at every  $0.6 \text{ m s}^{-1}$ , negative contours are dashed, zero contour is thickened). (c),(d) As in (a) and (b), but for hour 19. All fields are hourly and radially averaged over a 6 km radial range centered at the spiral shown in Fig. 8.

removing the azimuthal mean component. The environmental wind is computed by solving the following equation (Davis et al. 2008) over the innermost storm-following domain:

$$\begin{split} & \nabla^{2} \psi = \zeta, \quad \nabla^{2} \chi = \delta, \\ & \psi|_{\partial} = 0, \quad \chi|_{\partial} = 0, \\ & \mathbf{v}_{\psi} = \hat{k} \times \nabla \zeta, \quad \mathbf{v}_{v} = \nabla \chi, \quad \mathbf{v}_{\text{env}} = \mathbf{v}_{\text{ST}} - \mathbf{v}_{\psi} - \mathbf{v}_{v}, \end{split} \tag{2}$$

where  $\nabla^2$  is the horizontal Laplacian operator;  $\cdot|_{\partial}$  denotes evaluation at the boundary of the 1 km innermost domain;  $\zeta = \hat{k} \cdot \nabla \times \mathbf{v}_{\mathrm{ST}}$  and  $\delta = \nabla \cdot \mathbf{v}_{\mathrm{ST}}$  are the relative vorticity and divergence of the storm relative horizontal wind field  $\mathbf{v}_{\mathrm{ST}}$ ;  $\psi$  and  $\chi$  are streamfunction and velocity potential;  $\mathbf{v}_{\psi} = (u_{\psi}, v_{\psi})$  and  $\mathbf{v}_{\chi} = (u_{\chi}, v_{\chi})$  are the nondivergent and irrotational winds. As shown in Fig. 9b, the asymmetric storm tangential wind  $(v_a)$  follows the same descending trend as the wind acceleration in the DL quadrant. This, therefore, demonstrates that the storm tangential wind field is top-heavy in the DR, but bottom-heavy in the DL. The descending wind pattern is also found in the rainband complex simulated in a quiescent environment (Wang et al. 2019), indicating that this is common feature with a TC rainband complex.

At hour 19, the rainband has intensified to near its peak intensity. As shown in Fig. 9c, intense vertical updrafts extend more into the DL and span more uniformly the DR quadrant. The associated diabatic heating structure (Fig. 9d) is also significantly stronger than hour 17. In the downwind sectors of the rainband, weakening in both upward motion and diabatic heating is still clear but shifted more toward the downwind end (sector D–F).

Accompanying the structural changes in updrafts and diabatic heating, both the tangential wind acceleration and asymmetric tangential wind  $v_a$  in hour 19 show a clear downwind shift. The tangential wind acceleration becomes largely concentrated in the downwind sectors D-F (Fig. 9c), while the asymmetric tangential wind  $v_a$  displays a strong maximum that extends into sector E, peaking near 8 km altitude (Fig. 9d). Near sector E, the asymmetric  $v_a$  quickly descend toward the surface and the storm wind field becomes strongly bottom-heavy at sector F. At hour 19, the wind acceleration is mostly offset from the asymmetric wind, indicating that the asymmetric wind mostly reaches its peak intensity and axisymmetrization process of the wind field is underway. The dynamics of the wind acceleration along the rainband will be explored next.

#### 6. Quadrant-averaged tangential wind budget analysis

As demonstrated in the along-band analysis in section 5, during the intensification period of the quasi-stationary rainband, near and outside of the rainband is widespread tangential wind acceleration that extends from the upper levels of the DR quadrant toward the low levels of the DL (Fig. 9a). This acceleration is accompanied by descending asymmetric tangential wind within the rainband. To further understand the dynamics of this storm-scale wind acceleration, quadrant-averaged tangential wind budgets are performed to quantify the contributions of individual processes.

The quadrant-averaged tangential velocity equation [(A8) of appendix] is

$$\frac{\partial_{c}\overline{v}_{ST}}{\partial t} = -\frac{\overline{u}_{ST}}{r}\frac{\partial M_{ST}}{\partial r} - \frac{\overline{v}_{ST}}{r}\frac{\partial v_{ST}}{\partial \lambda} - \overline{w}\frac{\partial v_{ST}}{\partial z} - \frac{\overline{1}}{r\rho}\frac{\partial p}{\partial \lambda} + \overline{\overline{F_{\lambda}}} - \overline{fu_{c}} - \frac{\partial_{c}\overline{v}_{c}}{\partial z}, \tag{3}$$

where the overbar denotes quadrant averaging, and  $\mathbf{v}_c = (u_c, v_c)$  is the vector of storm translation. All other variables bear the same physical meaning as in Eq. (1). Note that our goal here is to investigate the quadrant-averaged acceleration from a dynamical perspective instead of looking at wavemean-flow interaction within the quadrant; therefore, in Eq. (3) we do not separate the nonlinear terms into mean and eddy contributions. We focus on selected quadrants at specific hours to highlight details of the ongoing dynamical processes.

#### a. Downshear-right quadrant at hour 17

We first examine the acceleration in the DR at hour 17. Figure 10 shows the corresponding quadrant-averaged tangential wind budget. The last two terms in Eq. (3) are both small and are therefore not shown. Figures 10b and 10c show a comparison between the actual and integrated tangential wind changes during this hour. Similar to results presented in section 4, the integrated tendency captures most of the acceleration pattern outside  $r = 20 \,\mathrm{km}$ .

Figure 10b shows that the DR quadrant in the low to midlevels experiences significant positive acceleration between 40 and 60 km radii. The pattern of the strongest acceleration is rather upright and radially confined. The major contribution of the tendency pattern comes from vertical advection (Fig. 10i) associated with the strong diabatic heating and convective updrafts located in this region (Fig. 3h). In addition to vertical advection, the horizontal advection is also positive below 3 km altitude (Fig. 10f). This positive tendency arises mostly from radial advection, which is due to low-level inflow at these radii (Figs. 10d,f). But this low-level horizontal advection pattern is slightly offset by the pressure gradient acceleration (Fig. 10g). Overall, vertical advection most dominantly shapes the total tangential acceleration in DR quadrant low to midlevels. This pattern significantly projects onto the axisymmetric acceleration, as suggested by the mean vertical advection of angular momentum (Fig. 6e).

#### b. Downshear-left quadrant at hour 17

We next examine the acceleration in the DL quadrant and compare with the concurrent DR fields at hour 17. As shown in Fig. 11a, during this 1-h period, the DL quadrant experiences an organized acceleration that covers from 40 km to near 120 km radii.

Figures 11b and 11c show that the widespread acceleration in DL has a clear slantwise pattern that descends from upper levels at outer radii toward low levels at inner radii, capturing the general pattern in Fig. 6a. Among the individual terms, the total horizontal advection (Fig. 11f) is the dominant contributor of this descending pattern, which is an outward-sloping

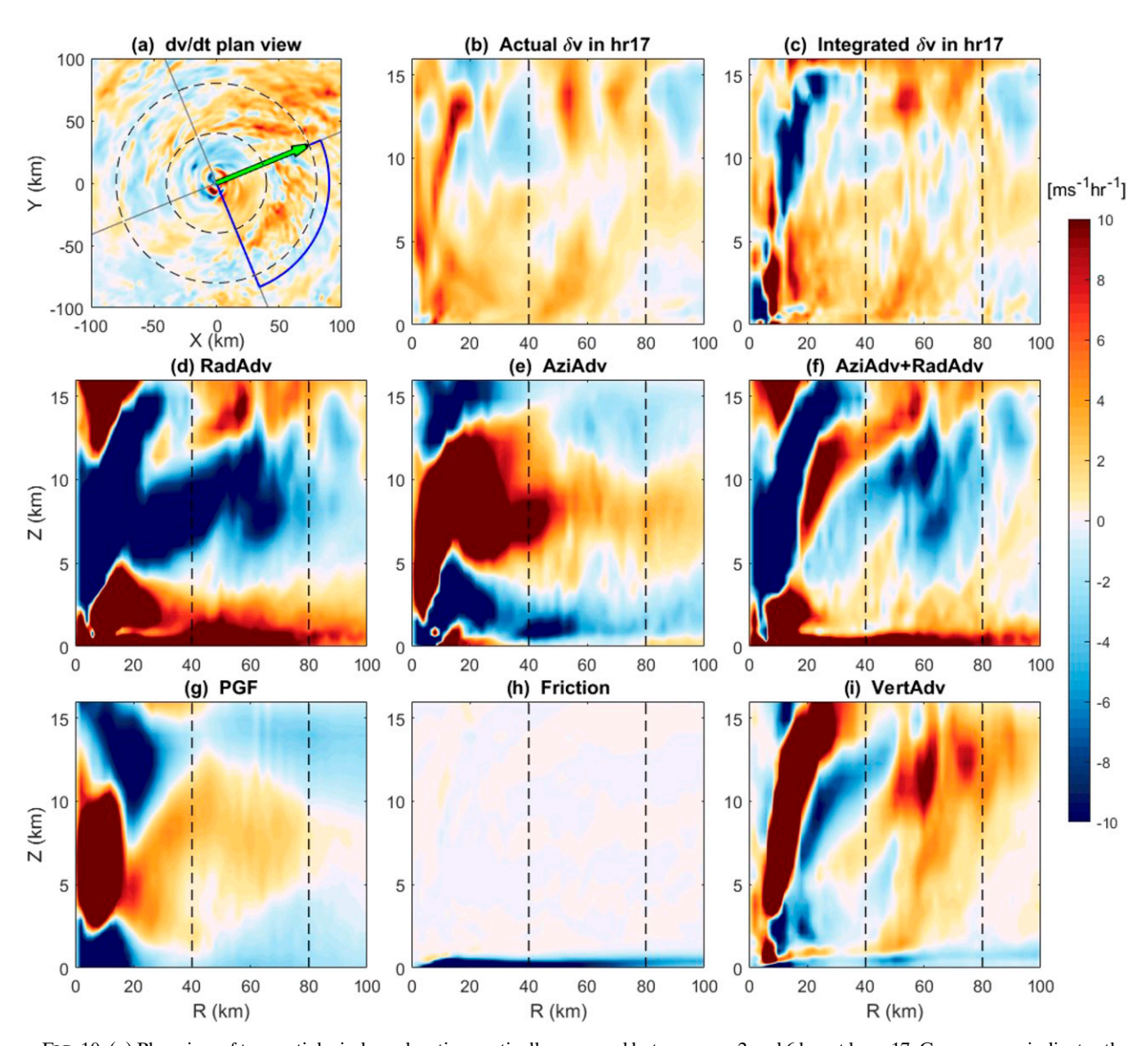


FIG. 10. (a) Plan view of tangential wind acceleration vertically averaged between z=2 and 6 km at hour 17. Green arrow indicates the 850–200 mb wind shear vector. Shear-relative quadrants are indicated by solid straight lines. Blue contour highlights the quadrant of interest. (b)–(i) The tangential wind budget averaged over the downshear-right (DR) quadrant: (b) the actual hourly changes in tangential wind, (c) the integrated hourly changes of tangential wind, (d) radial advection, (e) azimuthal advection, (f) total horizontal advection, (g) the contribution from pressure gradient force, (h) the contribution from boundary layer friction, and (i) the contribution from vertical advection. All vertical black dashed lines indicate 40 and 80 km radii.

band of acceleration covering 40 to 80 km radii. Both radial and azimuthal advection contribute positively to this acceleration band. Specifically, near 60 to 80 km radii, azimuthal advection is positive between 4 and 11 km altitudes. This positive azimuthal advection is in good agreement with the top-heavy wind structure (positive  $v_a$  above 5 km altitude, as in Fig. 9b) in the DR quadrant, which implies that high angular momentum air is transported from the upwind (DR) quadrant into the DL quadrant. Near the bottom and underneath the positive azimuthal advection, radial advection is positive, which indicates that angular momentum is drawn inward by the radial inflow below 4 km altitude near 40 to 70 km radii, as shown in Fig. 11d.

To further understand the origin of this midlevel radial inflow, we decompose the radial velocity into irrotational  $(u_\chi)$ , nondivergent  $(u_\psi)$  and environmental  $(u_{\rm env})$  components using Eq. (2), as shown in Figs. 12e-h. As expected, the environmental  $u_{\rm env}$  (Fig. 12h) is largely uniform in the horizontal direction, with structure consistent with the direction of the environmental wind shear. As shown in Figs. 12e and 12f, the midlevel inflow (near  $z=4\,{\rm km}$ ) between 40 and 70 km radii receives a large contribution from the irrotational radial inflow (Fig. 12f). This midlevel irrotational inflow begins radially outward of the stratiform diabatic forcing at midlevels (contours in Fig. 12f), with its inner edge collocated with

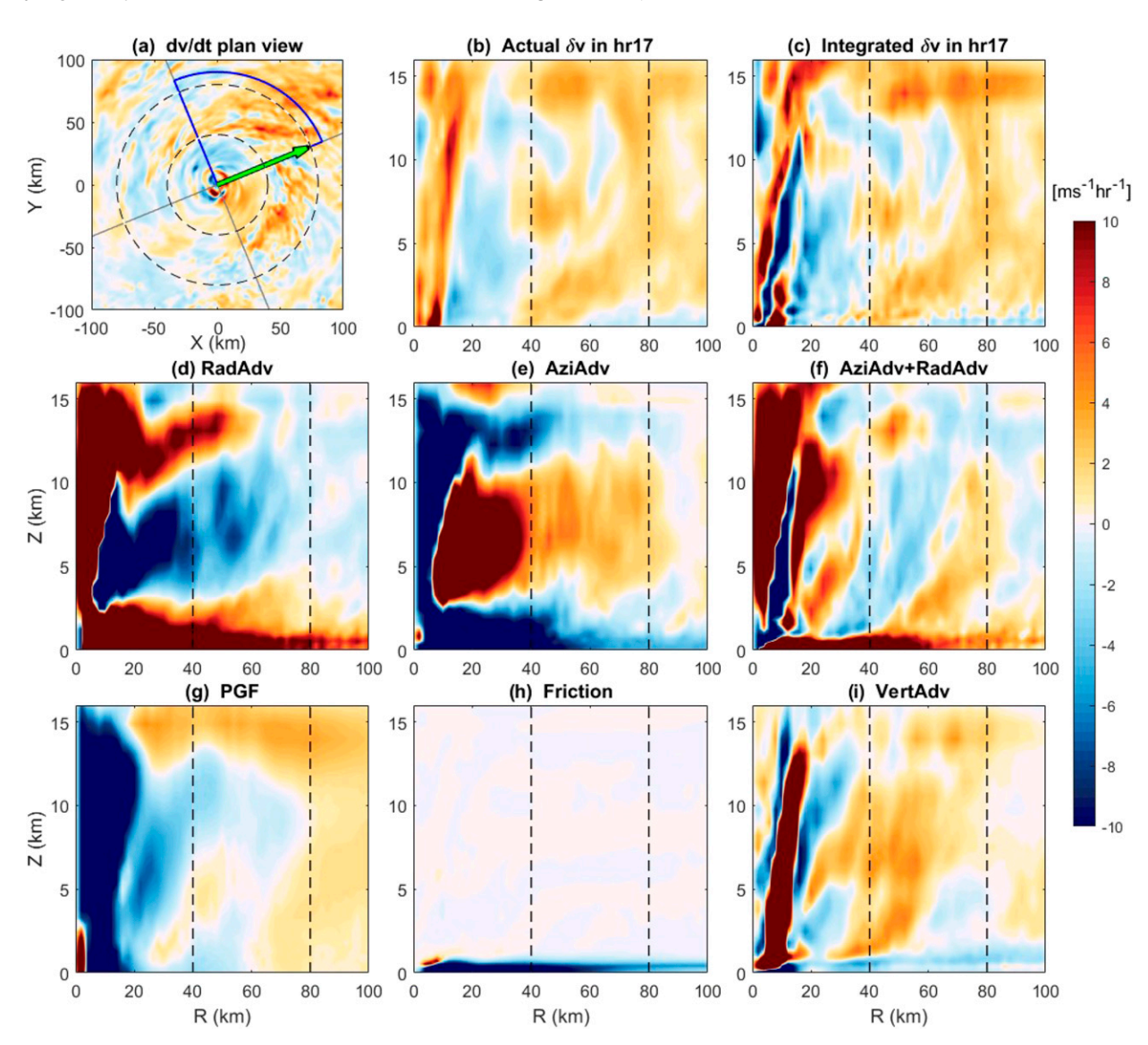


FIG. 11. As in Fig. 10, but for downshear-left (DL) quadrant at hour 17.

cooling and downdraft (dashed contour in Fig. 12e), and thus resembles the MDI (Didlake and Houze 2013). In contrast, the low-level irrotational inflow in DR (Fig. 12b) resides outward of convective heating patterns. Thus, we see clearly that the irrotational inflows in these two quadrants are driven by convergence associated with distinct diabatic heating/cooling structures. Looking back at Figs. 11d and 11f, the stratiform-induced MDI also appears associated with the inward radial advection and the outward sloping band of positive horizontal acceleration in the same region.

The vertical advection in the DL quadrant (Fig. 11i) also contributes positively to the tangential wind tendency due to the corresponding deep updrafts seen in Fig. 12e. These updrafts all populate the inner edges of the rainband and are located immediately inward of the aforementioned descending inflow near 40 to 60 km radii (Fig. 11f). However, at this early phase of SEF, a large portion of these updrafts undergo

outward acceleration once they leave the boundary layer, thus resulting in a near cancellation with the total horizontal advection due to angular momentum conservation. The net effect of this cancellation, together with the contribution from pressure gradient force term, is a relatively weak positive contribution at the inner edge of the aforementioned acceleration band (Figs. 11c,f). Overall, the findings in sections 6a and 6b suggest that the distinct acceleration patterns in DR and DL in hour 17 are indeed due to the two different acceleration processes.

## c. Upshear-left quadrant at hour 19

As discussed in section 4, hour 19 is the earliest hour when the main region of tangential wind acceleration extends from the downshear quadrants toward the upshear quadrants (Fig. 5f). It, therefore, marks the beginning of the axisymmetrization of the wind acceleration of the secondary

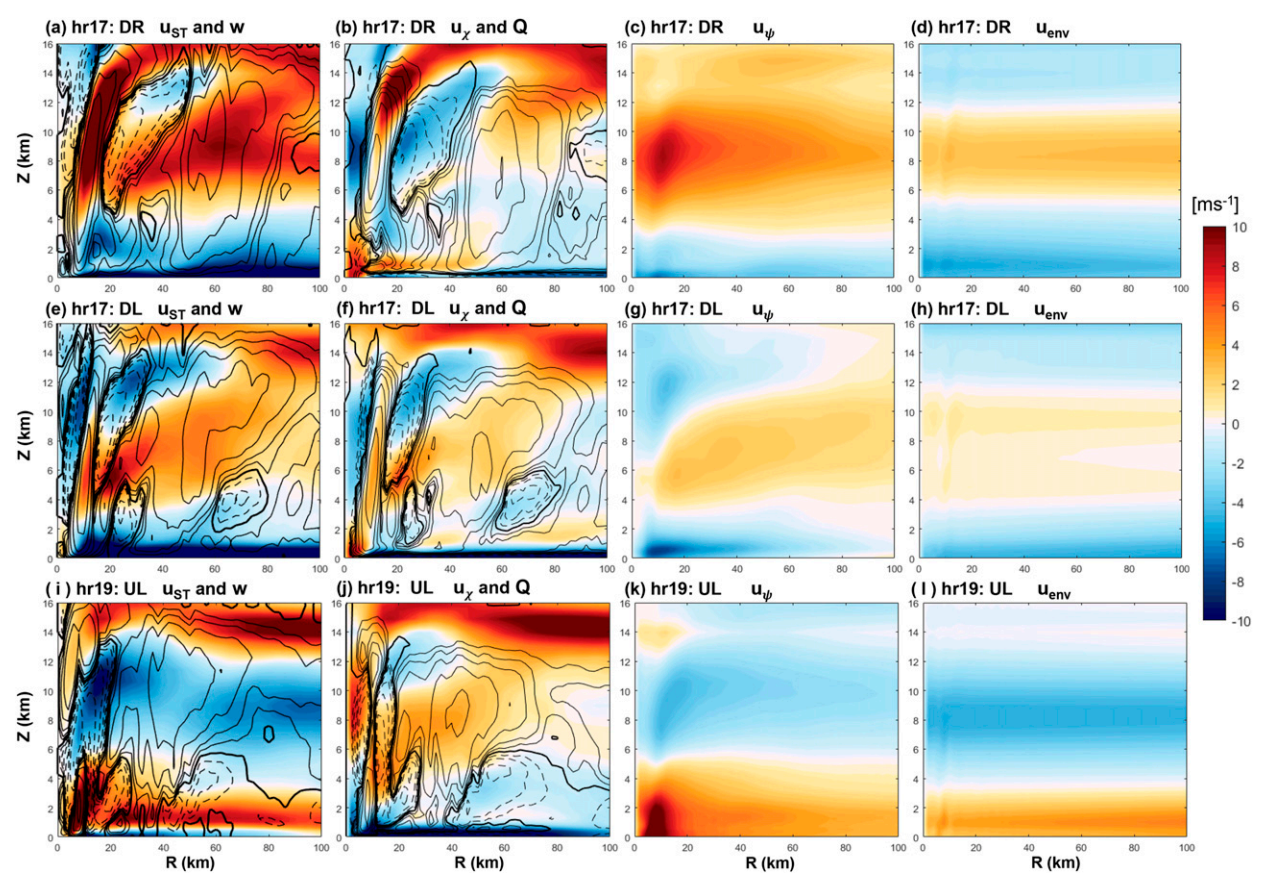


FIG. 12. Quadrant and hourly averaged radial velocity and its flow components. (a) Storm-relative radial velocity  $u_{\rm ST}$  (shading) and vertical velocity w (contoured at  $\{0, \pm 1, \pm 2, \pm 4, \dots, \pm 64\} \times 0.08\,\mathrm{m\,s^{-1}}$  with  $0\,\mathrm{m\,s^{-1}}$  thickened) in the DR quadrant at hour 17. (b) Irrotational component  $u_{\chi}$  (shading) and diabatic forcing (contoured at every  $\{0, \pm 1, \pm 2, \pm 4, \dots, \pm 64\} \times 2.5 \times 10^{-4}\,\mathrm{K\,s^{-1}}$  with  $0\,\mathrm{K\,s^{-1}}$  thickened). (c) Nondivergent component  $u_{\psi}$ . (d) Environmental component  $u_{\mathrm{env}}$ . (e)–(h) As in (a)–(d), but for DL quadrant at hour 17. (i)–(l) As in (a)–(d), but for UL quadrant at hour 19.

eyewall. Figure 13 shows the tangential wind budget during this hour in the UL quadrant. As can be seen in Figs. 13b and 13c, near 30 km radius, there is a band of wind acceleration that extends vertically from the boundary layer to 10 km altitude. At outer radii, a broad but weaker positive acceleration covers outside of 60 km radius.

Vertical advection is an important contributor to the total acceleration pattern near 30 km. Here, organized updrafts bring high tangential momentum air from the boundary layer to the free troposphere, resulting in a clear peak of tangential acceleration outside of the primary eyewall. Another important contribution of the acceleration near 30 km radius is the pressure gradient force term, which accelerates the tangential wind below 5 km. This positive pressure gradient force is due to the buildup of asymmetric high pressure in the DL quadrant (not shown) owing to hydrostatic adjustment to stratiform cooling.

Horizontal advection (Fig. 13f) also has important contributions to the total tendency in this quadrant. Above 3 km and near 30 km radius, the horizontal advection term shows a positive contribution, which is also a major contribution to the acceleration of the incipient secondary eyewall. Outside of 40 km radius, positive horizontal acceleration extends beyond

100 km radius. This storm-scale acceleration has a descending pattern toward inner radii and seemingly connects to the boundary layer at the outer edge of the updraft region of the developing secondary eyewall. While this acceleration is partially offset by the vertical advection term, its general pattern remains in the total tangential wind tendency.

#### d. Decomposing the horizontal advection of tangential wind

In the previous quadrant analyses, horizontal advection of tangential wind has a major contribution in the total tangential wind acceleration in each quadrant. However, when looking into the radial and azimuthal advections in the UL quadrant (Figs. 13d,e), we found that these two terms have strong cancellation in various regions. Such cancellation is due to the wind field asymmetry, which results in projection of M-conserving flow onto both the radial and tangential directions. As confirmed in Figs. 12i–l, the radial flow in the UL quadrant has an upper-level inflow, lower-level outflow structure that largely comes from the nondivergent ( $u_{\psi}$ ) and environmental ( $u_{\rm env}$ ) components. These two components obscure the midlevel irrotational inflow ( $u_{\chi}$ ) that is collocated with both the stratiform cooling (contours in Fig. 12j) and the positive horizontal

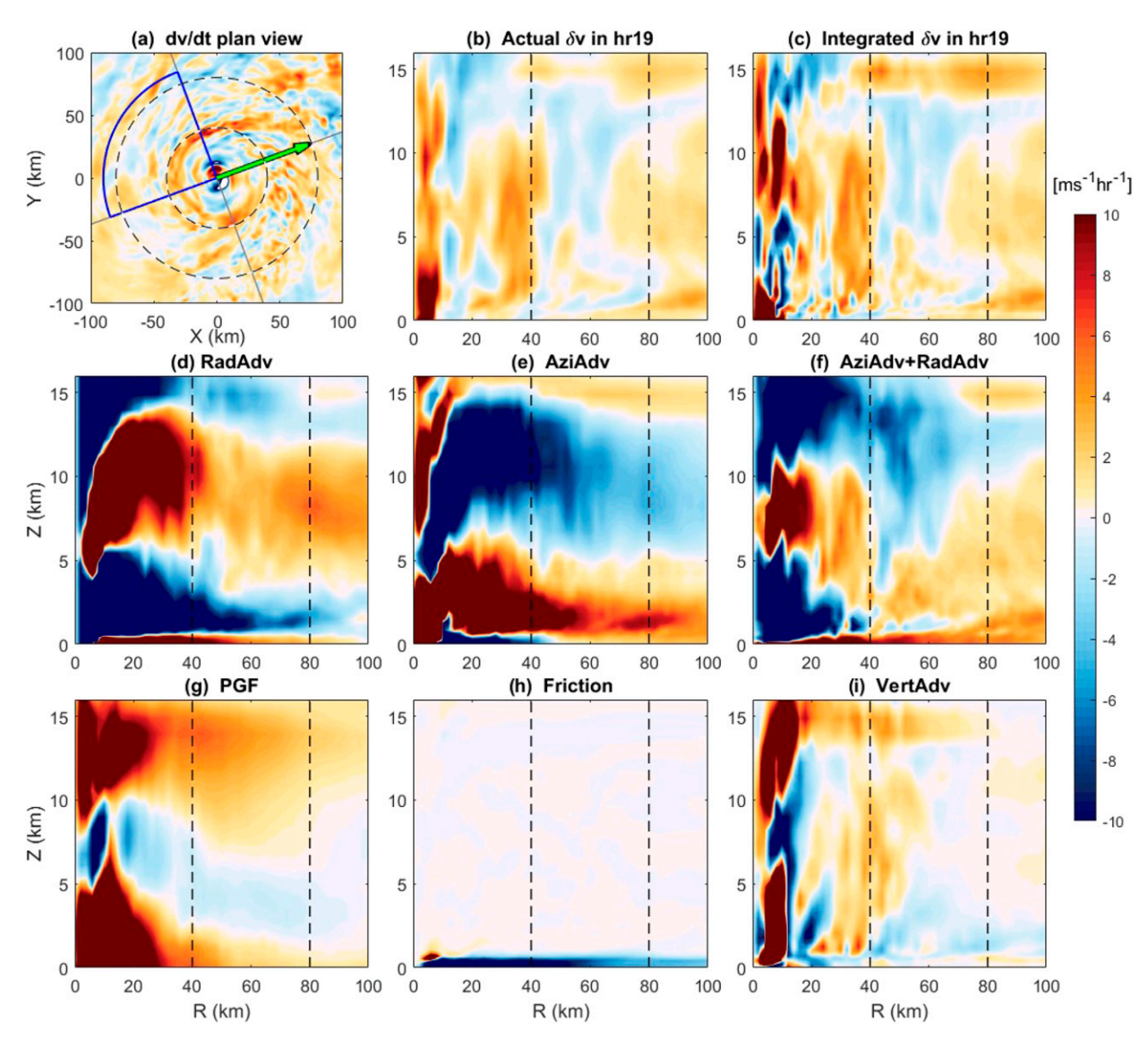


FIG. 13. As in Fig. 10, but for upshear-left (UL) quadrant at hour 19.

advection (Fig. 13f). Therefore, examining the irrotational and nondivergent winds, rather than radial and tangential components, may further help inform our current analysis on the horizontal advection of the tangential wind and link these patterns to convection processes.

Furthermore, it was also shown in Figs. 6d and 7d that the mean radial advection [i.e.,  $-\overline{u}_{\rm ST}(\partial \overline{M}_{\rm ST}/\partial r)$ ] has an important contribution to the azimuthal mean tangential wind acceleration. Using Green's theorem, we know that  $\overline{u}_{\rm ST} = \overline{u}_{\chi}$  since both  $u_{\psi}$  and  $u_{\rm env}$  are divergence-free:

$$\overline{u}_{ST} = \frac{1}{2\pi r} \oint \mathbf{v}_{ST} \cdot \hat{r} \, r \, d\lambda = \frac{1}{2\pi r} \iint \nabla \cdot \mathbf{v}_{ST} \, dA$$

$$= \frac{1}{2\pi r} \iint \nabla \cdot \mathbf{B}_{\chi} \, dA = \overline{u}_{\chi}. \tag{4}$$

This means that the mean radial advection  $-\overline{u_{ST}}(\partial \overline{M_{ST}}/\partial r)$  only receives contribution from the irrotational radial velocity

 $\overline{u}_{\chi}$ . Therefore, it is useful to further quantify the contribution of irrotational wind to the horizontal advection in different quadrants.

We decompose the horizontal advection into the advection by irrotational and nondivergent flows:

Horizontal advection = 
$$-\frac{\mathbf{v}_{\text{ST}}}{r} \cdot \nabla M_{\text{ST}}$$
  
=  $-\frac{\mathbf{v}_{\chi}}{r} \cdot \nabla M_{\text{ST}} - \frac{\mathbf{v}_{\psi}}{r} \cdot \nabla M_{\text{ST}}$ . (5)

Here, we have grouped the nondivergent  $\mathbf{v}_{\psi}$  and environmental  $\mathbf{v}_{\text{env}}$  components into  $\mathbf{v}_{\psi}$ , which is still divergence-free. Figure 14 shows the decomposition of the horizontal advections of the three selected quadrants/times. Figures 14c, 14g, and 14k show that the advection by the nondivergent wind  $\mathbf{v}_{\psi}$  is significant in the quadrant averages. This tendency can only contribute in an axisymmetric sense to the radial eddy fluxes

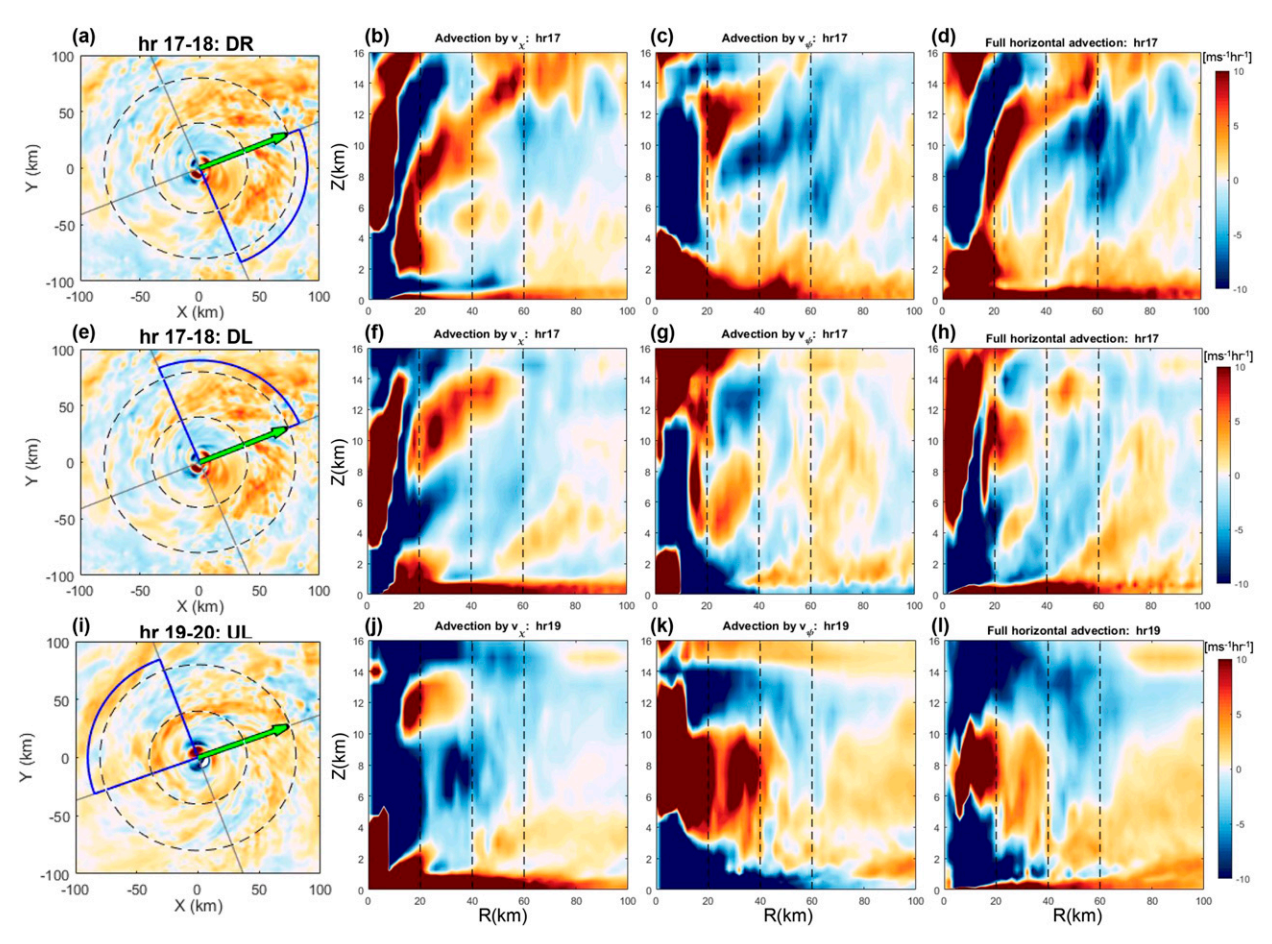


FIG. 14. The decomposition of horizontal advection. (a) Plan view of vertically averaged (z = 2-6 km) tangential wind acceleration in DL quadrant at hour 17. Green arrow indicates shear vector (850–200 mb) and blue solid contour indicates the quadrant of interest. (b) Quadrant-averaged advection by the irrotational wind. (c) Quadrant-averaged advection by nondivergent wind. (d) Quadrant-averaged total horizontal advection in DL at hour 17. (e)–(h) As in (a)–(d), but for DL quadrant at hour 17. (i)–(l) As in (a)–(d), but for UL quadrant at hour 19.

(Figs. 6g and 7g), which appear to play a role in the total angular momentum tendency at the top of the boundary layer. Consistent with Figs. 12b and 12f, which demonstrated the distinct driving forces of the irrotational flows in DR and DL, here in Figs. 14b and 14f we can further see how the difference in their driving forces result in the distinct patterns in their contribution to the axisymmetric wind acceleration. The irrotational flow in the DR is driven by convergence (not shown) underneath convective heating near 40 to 60 km radii; thus, its contribution resides mostly in the lower troposphere and near surface (Fig. 14b). On the other hand, the irrotational flow in the DL (Fig. 12f) is driven by the midlevel convergence induced by the stratiform diabatic forcing. As this irrotational inflow passes through stratiform cooling near 4km altitude, it becomes negatively buoyant (Yu and Didlake 2019) and forms an MDI, which draws angular momentum inward (Fig. 14f) and results in the descending trend in the acceleration pattern (Fig. 14h). At the beginning of axisymmetrization at hour 19, the stratiform cooling in UL (Fig. 12j) is more pronounced, and so is the MDI. The MDI seemingly connects to the boundary layer at its inner edge and has important contribution to the horizontal advection (Fig. 141). This analysis demonstrates that the irrotational flow, specifically the MDI induced by the stratiform diabatic forcings, indeed plays an important role in shaping and initiating the descending storm-scale wind acceleration in the left-of-shear half of the storm and contributing to the axisymmetric wind acceleration.

## 7. Evolution of MDI

Given the importance of the MDI shown at hours 17 and 19, we next examine the prominence and evolution of this pertinent feature. Based on Fig. 12, we note that this MDI feature is best identified with the negative irrotational radial velocity coinciding with sinking motion. Therefore, we examine the joint frequency distributions of  $u_{\chi}$  and w in each quadrant from hours 16 to 20 (Figs. 15a–d). These joint frequency plots are created by first applying a 30° azimuthal moving average to the  $u_{\chi}$  and w fields (in cylindrical coordinates) to filter out

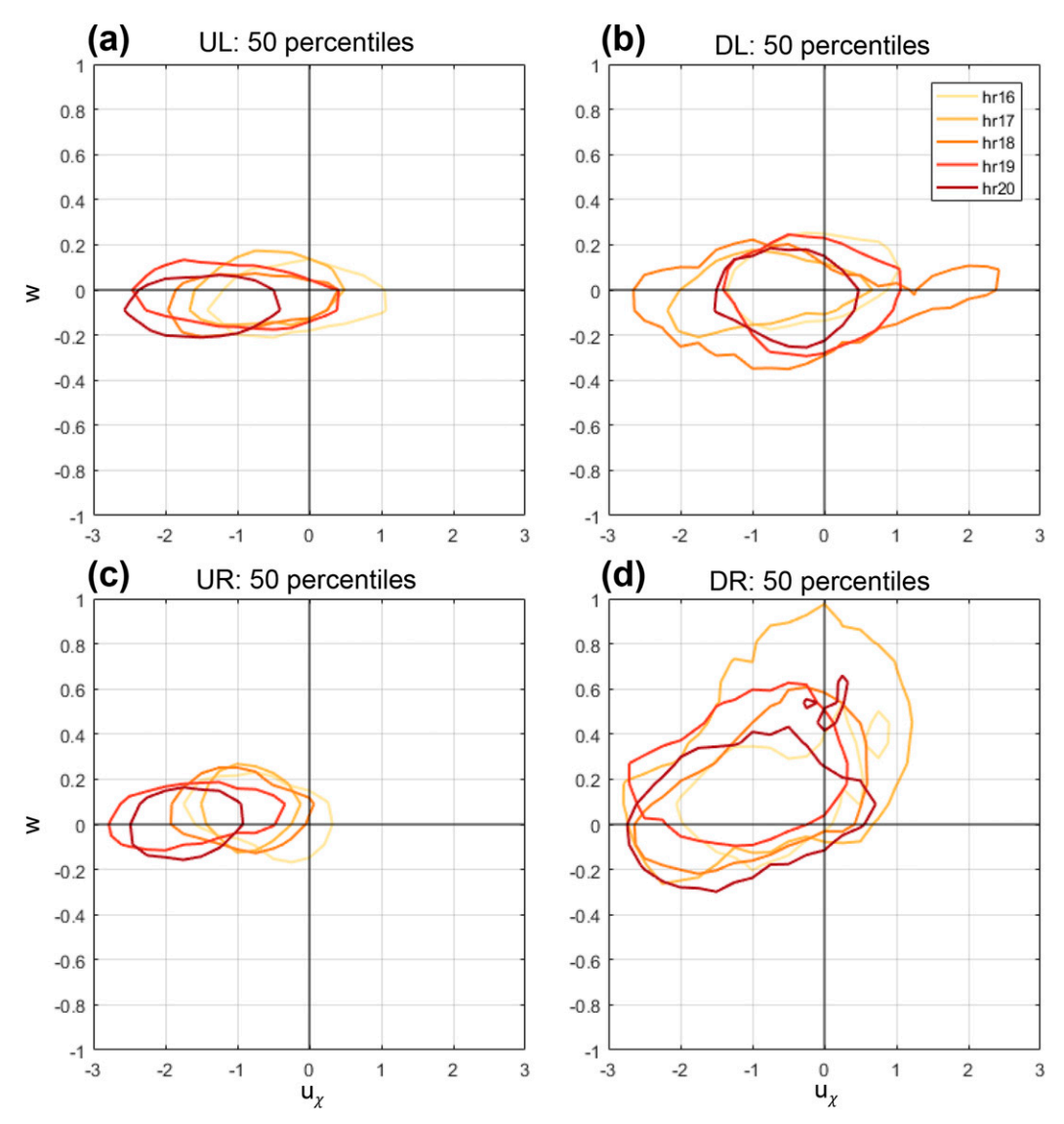


FIG. 15. Normalized joint frequency distributions of 30° azimuthally averaged  $u_{\chi}$  and w between r=40 to 80 km and from z=2 to 6 km during hours 16 to 20 for (a) UL, (b) DL, (c) UR and (d) DR. Only the 50th-percentile contour lines for each hour are shown.

small-scale waves and to extract the mesoscale signals. Then, all data pairs of  $(u_\chi, w)$  between  $40-80\,\mathrm{km}$  radius and  $2-6\,\mathrm{km}$  altitude in each quadrant are counted for each hour separately. Note that data pairs at smaller radii are distributed more densely, representing smaller volumes. Therefore, the count for each data pair is weighted by its differential volume  $(r \times dr \times dz)$ . The resulting distribution at each hour is then normalized by the peak value of the distribution. In Figs. 15a–d, only the 50th-percentile contours are plotted.

Among the quadrants, the distributions in the DR are most widespread and largely have positive w and negative  $u_{\chi}$  due to the vigorous convective rainband activity. Downwind in the DL quadrant, occurrences of negative w and negative  $u_{\chi}$  have a more significant contribution to the distributions starting from hour 17, suggesting the existence of an MDI. The UL quadrant

also has more distribution centered in the diagram space of negative w and  $u_x$ .

To further demonstrate the spatial and temporal evolution of the MDI, we focus on the lower-half plane of the  $u_\chi$ –w phase diagram and show the azimuth–time evolution of the  $u_\chi$  (shading) and negative w (contour) in Fig. 16a, and the tangential wind acceleration (shading) and irrotational wind contribution ( $-u_\chi \zeta_a$ , contour) in Fig. 16b. To create these figures, an additional 30-min averaging is applied to these fields. Then for each azimuth, the data points that satisfy a downdraft threshold of  $-0.075\,\mathrm{m\,s^{-1}}$  (i.e.,  $\langle w \rangle_{30\mathrm{min}} < -0.075\,\mathrm{m\,s^{-1}}$ ) are integrated along the radius (r=40–80 km) and height dimensions (z=2–6 km) and normalized by the integrated volume ( $80\,\mathrm{km^2}-40\,\mathrm{km^2}$ )(6 km  $-2\,\mathrm{km}$ ). The downdraft threshold of  $-0.075\,\mathrm{m\,s^{-1}}$  is simply to exclude downdrafts that are too

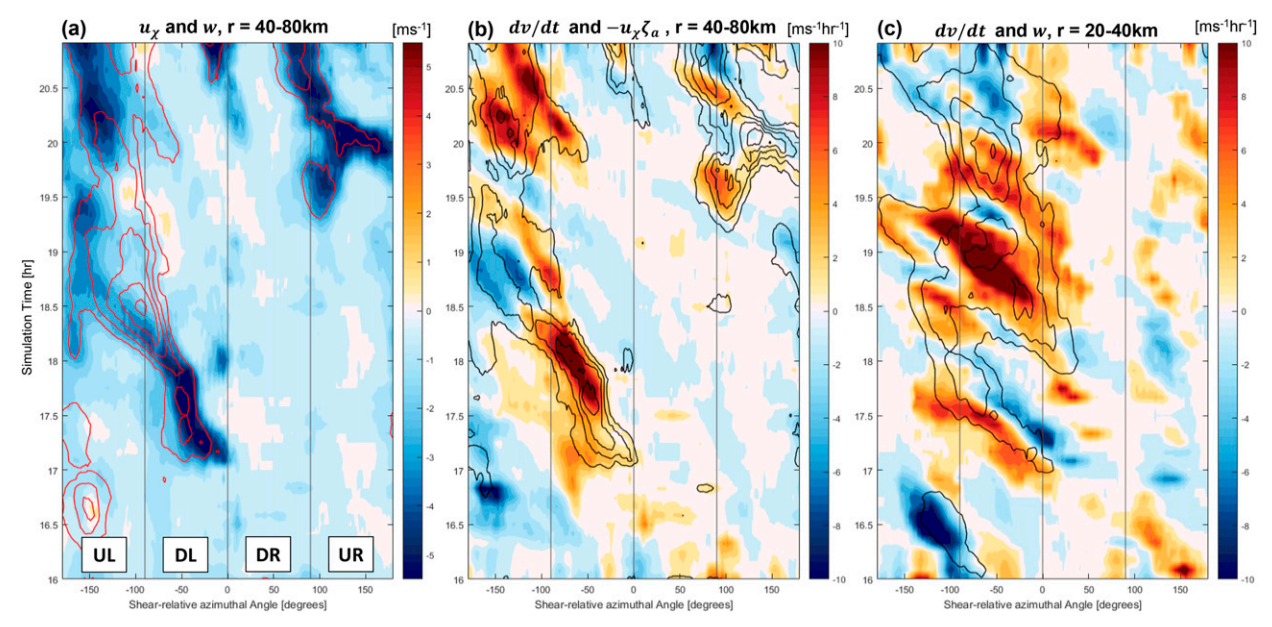


FIG. 16. The azimuthal and time evolution of (a)  $u_{\chi}$  (shading) and w (contoured in red every  $-0.3\,\mathrm{m\,s^{-1}}$  from  $-0.3\,\mathrm{to}-1.5\,\mathrm{m\,s^{-1}}$ ) and (b) tangential wind acceleration (shading) and irrotational wind contribution ( $-u_{\chi}\xi_a$ ; contoured in black every  $1.5\,\mathrm{m\,s^{-1}}\,h^{-1}$  from  $1.5\,\mathrm{to}$  9 m s<sup>-1</sup> h<sup>-1</sup>) for data that satisfy the criterion of  $\langle w \rangle_{30\mathrm{min}} < -0.075\,\mathrm{m\,s^{-1}}$  between 40 and 80 km radii. (c) As in (a) and (b), but for tangential wind acceleration (shading) and updraft (contoured in black every  $0.8\,\mathrm{m\,s^{-1}}$  from  $0.8\,\mathrm{to}$  4 m s<sup>-1</sup>) between 20 and 40 km radii where data satisfy the criterion of  $\langle w \rangle_{30\mathrm{min}} > 0.075\,\mathrm{m\,s^{-1}}$ .

weak to be representative of the existence of MDI. From Fig. 16a, it is clear that the majority of strong downdrafts (red contours) correspond well with negative  $u_x$ , indicating existence of an MDI. A clear MDI feature first emerges at the DL quadrant at hour 17, which also coincides (both temporally and spatially) with the emergence of broad wind acceleration shown in Figs. 5e and 16b. This wind acceleration region (Fig. 16b, shading) receives substantial contribution from irrotational inflow  $(-u_{\chi}\zeta_{a}, \text{ contoured})$ , demonstrating that the MDI indeed plays an important role in the early acceleration of the wind field by drawing absolute vorticity toward the lower troposphere and boundary layer (as w < 0 at MDI region). During hours 18 and 19, the MDI feature propagates downwind and remains persistent in the UL quadrant where it interacts with the boundary layer (Fig. 12e), and later extends to the UR at hour 20. This progression is also consistent with the lags in the downwind shift of the 50th-percentile contours toward the negative w and  $u_x$  space between UL and DL (Figs. 15a,b).

In Fig. 16c, we also show the azimuthal evolution of the tangential wind acceleration (shading) and updraft (contour) at the inner radii between 20 and 40 km. Consistent with previous analysis discussed in section 6c, significant wind acceleration at 20–40 km radius occurs in the DL quadrant around hour 18. This organized wind acceleration is collocated with notable updrafts, suggesting that vertical advection is an important contributor to the acceleration at the inner radii. These inner updrafts appear around the same time when the downwind MDI advances into the UL quadrant (Figs. 16a,b). These patterns are consistent with the finding of Yu and Didlake (2019) that cooling from a stationary stratiform rainband is capable of triggering intense updrafts at its radially inward and

upwind side. More detailed analyses on the coupling mechanism between the MDI and these intense updrafts will be performed in a subsequent study.

#### 8. Conclusions

In this study, we investigated the detailed dynamics of the evolving tangential wind field prior to and during a secondary eyewall formation (SEF) event in a convection-permitting model simulation of Hurricane Matthew (2016). We focus primarily on the role that asymmetric rainband processes have on the local and axisymmetric tangential wind acceleration. Embedded in moderate environmental wind shear, the simulated storm develops a rainband complex that remains largely stationary in the downshear quadrants prior to SEF. As this rainband complex intensifies, the TC wind field experiences a broadening of the axisymmetric tangential wind field associated with the rainband complex. Soon after, a low-level axisymmetric wind maximum develops within the incipient secondary eyewall. We highlight specific times of the simulation that correspond to the intensification period of this rainband complex (hour 17) and also the initial axisymmetrization stage that leads to SEF (hour 19).

At hour 17, the angular momentum axisymmetric tendency field has an inward-descending positive tendency pattern that extends from 120 to 50 km radii and maximizes at low levels. Mean vertical advection contributes to a more concentrated positive tendency region near 50 km radius, while mean radial advection is more widespread and captures the overall descending pattern, indicating the possibility of having distinct modes of tangential acceleration.

A close examination of the tangential acceleration field reveals distinct characteristics in different quadrants of the storm. In the downshear-right (DR) quadrant where the rainband complex is more convective, the acceleration is more upright and concentrates within a band of 20 km wide centered at 50 km radius. A quadrant-averaged tangential wind budget over the DR confirms that vertical advection is the dominant contributor here, resulting in a local acceleration pattern that resembles the mean vertical advection in the aforementioned angular momentum budget.

In the downshear-left (DL) quadrant, the acceleration is similarly intense but more widespread, extending from 40 to 120 km radius. Here, horizontal advection plays a more important role in shaping the total acceleration structure than vertical advection. This horizontal advection is a slantwise band of positive acceleration, with azimuthal import of high angular momentum air at the upper levels and inward advection of angular momentum by a persistent midlevel inflow underneath. This midlevel inflow is collocated with diabatic cooling and downward motion, resembling the mesoscale descending inflow (MDI) that has been examined in observational studies (Didlake and Houze 2013; Didlake et al. 2018). This emergence of the MDI in the DL quadrant is also the primary reason of the inwarddescending pattern in the axisymmetric acceleration outside of 40 km radius. By decomposing the horizontal flow into irrotational and nondivergent components, we show that this MDI is best identified with the irrotational velocity as irrotational inflow coinciding with sinking motion. This feature, closely associated with diabatic cooling in stratiform precipitation, suddenly emerges at hour 17 in the DL quadrant, consistent with the timing and location of the first appearance of the widespread tangential acceleration there.

By tracking the evolution of downdrafts, we show that throughout the SEF period, the MDI strengthens and travels downwind over time. As the MDI traverses into the upshearleft (UL) quadrant at hour 19, it becomes more widespread, and so as the associated acceleration at large radii. We note that the UL is also the quadrant where the MDI seemingly interacts with the boundary layer. At the inner edge of the descending inflow, new convective updrafts are triggered, which are found to be important to the axisymmetric tangential acceleration at low levels and the following axisymmetrization of the secondary eyewall. This stratiform-to-convective transition is also similar to the observed pattern in Didlake et al. (2018). The exact processes governing the axisymmetrization of convection to form the secondary eyewall in this simulation will be examined in a subsequent study.

Several aspects of this study, such as the coupling between the troposphere and the boundary layer, require further examination. Furthermore, the features examined in this study highlight a single pathway for secondary eyewall formation from a stationary rainband complex in sheared tropical cyclones. Future studies need to examine whether similar dynamical processes occur generally in SEF of other TCs.

Acknowledgments. We thank Robert Fovell and Tsz-Kin Lai for their thoughtful comments on this study. We also thank the anonymous reviewers whose comments led to significant

improvements in the manuscript. This research was supported by the National Aeronautics and Space Administration under Grants NNX16AI21G (New Investigator Program) and 17-EARTH17F-184 under the NASA Earth and Space Science Fellowship Program, and by the National Science Foundation under Grants AGS-1810869 and AGS-1854607.

#### **APPENDIX**

#### **Storm-Relative Tangential Momentum Budget**

Storm-relative tangential wind budgets are often calculated in many studies by adapting the cylindrical coordinate tangential momentum equation to storm-relative tangential winds. But such an approach does not fully account for the effect of storm motion. Here, we rederive the storm-relative tangential wind momentum equation, with particular interest in using for storm sector budget calculations and for storms with appreciable translation speed. We begin with horizontal momentum equation

$$\frac{D\mathbf{v}}{Dt} = -\frac{1}{\rho}\nabla p - f\hat{\mathbf{k}} \times \mathbf{v} + \mathbf{F},\tag{A1}$$

where  $D/Dt = \partial/\partial t + \mathbf{v} \cdot \nabla + w(\partial/\partial z)$  is Lagrangian derivative; vector  $\mathbf{v} = (u, v)$  is the horizontal wind, with u and v being the radial and tangential components;  $\mathbf{F}$  is the external forcing. Next, defining the storm-following local time derivative as  $\partial_c/\partial t = \partial/\partial t + \mathbf{v}_c \cdot \nabla$ , where  $\mathbf{v}_c = (u_c, v_c)$  is the storm translation vector, Eq. (A1) becomes

$$\frac{\partial_c \mathbf{v}}{\partial t} = -(\mathbf{v} - \mathbf{v}_c) \cdot \nabla \mathbf{v} - w \frac{\partial \mathbf{v}}{\partial z} - \frac{1}{\rho} \nabla p - f \hat{\mathbf{k}} \times \mathbf{v} + \mathbf{F}.$$
 (A2)

We then take the dot product of (A2) with the unit vector along the azimuthal unit vector  $\hat{\lambda}$ :

$$\frac{\partial_c \mathbf{v}}{\partial t} = -\left[ (\mathbf{v} - \mathbf{v}_c) \cdot \nabla \mathbf{v} \right] \cdot \hat{\mathbf{\lambda}} - w \frac{\partial \mathbf{v}}{\partial z} - \frac{1}{r\rho} \frac{\partial p}{\partial \lambda} - fu + F_{\lambda}.$$
 (A3)

Using product rule,  $-[(\mathbf{v} - \mathbf{v}_c) \cdot \nabla \mathbf{v}] \cdot \hat{\boldsymbol{\lambda}}$  can be rewritten into two terms:

$$-[(\mathbf{v} - \mathbf{v}_{2}) \cdot \nabla \mathbf{v}] \cdot \hat{\boldsymbol{\lambda}} = -(\mathbf{v} - \mathbf{v}_{2}) \cdot \nabla \boldsymbol{v} + (\mathbf{v} - \mathbf{v}_{2}) \cdot \nabla \hat{\boldsymbol{\lambda}} \cdot \mathbf{v}. \tag{A4}$$

The second term arises due to curvature of the polar coordinate

$$(\mathbf{v} - \mathbf{v}_c) \cdot \nabla \hat{\mathbf{\lambda}} \cdot \mathbf{v} = \left[ (u - u_c) \frac{\partial \hat{\mathbf{\lambda}}}{\partial r} + \frac{(v - v_c)}{r} \frac{\partial \hat{\mathbf{\lambda}}}{\partial \lambda} \right] \cdot \mathbf{v} = -\frac{(v - v_c)}{r} u,$$
(A5)

where we use the fact that  $\partial \hat{\lambda}/\partial r = 0$  and  $\partial \hat{\lambda}/\partial \lambda = -\hat{\mathbf{r}}$ . Hence,

$$\frac{\partial_{c} \mathbf{v}}{\partial t} = -(\mathbf{v} - \mathbf{v}_{c}) \cdot \nabla \mathbf{v} - \frac{(\mathbf{v} - \mathbf{v}_{c})}{r} \mathbf{u} - \mathbf{w} \frac{\partial \mathbf{v}}{\partial z} - \frac{1}{r\rho} \frac{\partial p}{\partial \lambda} - f\mathbf{u} + F_{\lambda}.$$
(A6)

Defining storm-relative wind as  $\mathbf{v}_{ST} = \mathbf{v} - \mathbf{v}_c = (u_{ST}, v_{ST})$  and storm-relative absolute angular momentum as  $M_{ST} = rv_{ST} + (1/2)fr^2$ , (A6) may be rewritten as

$$\begin{split} \frac{\partial_{c} v_{\text{ST}}}{\partial t} &= -\frac{u_{\text{ST}}}{r} \frac{\partial M_{\text{ST}}}{\partial r} - \frac{v_{\text{ST}}}{r} \frac{\partial v_{\text{ST}}}{\partial \lambda} - w \frac{\partial v_{\text{ST}}}{\partial z} + \\ & \left[ -\frac{v_{\text{ST}}}{r} u_{c} - \frac{v_{\text{ST}}}{r} \frac{\partial (v_{c})}{\partial \lambda} \right] - \frac{1}{r\rho} \frac{\partial p}{\partial \lambda} + F_{\lambda} - f u_{c} - \frac{\partial_{c} v_{c}}{\partial t}. \end{split} \tag{A}$$

Note that because  $\partial(v_c)/\partial\lambda = \partial(\mathbf{v}_c \cdot \hat{\boldsymbol{\lambda}})/\partial\lambda = \mathbf{v}_c \cdot \partial(\hat{\boldsymbol{\lambda}})/\partial\lambda = -\mathbf{v}_c \cdot \hat{\mathbf{r}} = -u_c$ , the two terms inside the square bracket cancel. Equation (3) in section 6 is derived by taking sector averages to Eq. (A7):

$$\begin{split} \frac{\partial_{c}\overline{\overline{v}}_{ST}}{\partial t} &= -\frac{\overline{u}_{ST}}{r}\frac{\partial M_{ST}}{\partial r} - \frac{\overline{v}_{ST}}{r}\frac{\partial v_{ST}}{\partial \lambda} - \overline{w}\frac{\partial v_{ST}}{\partial z} - \frac{\overline{1}}{r\rho}\frac{\partial p}{\partial \lambda} \\ &+ \overline{\overline{F_{\lambda}}} - \overline{\overline{fu_{c}}} - \frac{\partial_{c}\overline{\overline{v}_{c}}}{\partial t}. \end{split} \tag{A8}$$

#### REFERENCES

- Abarca, S. F., and M. T. Montgomery, 2013: Essential dynamics of secondary eyewall formation. *J. Atmos. Sci.*, 70, 3216–3230, https://doi.org/10.1175/JAS-D-12-0318.1.
- Bell, M. M., M. T. Montgomery, and W. C. Lee, 2012: An axisymmetric view of concentric eyewall evolution in Hurricane Rita (2005). J. Atmos. Sci., 69, 2414–2432, https://doi.org/ 10.1175/JAS-D-11-0167.1.
- Black, M. L., and H. E. Willoughby, 1992: The concentric eyewall cycle of Hurricane Gilbert. *Mon. Wea. Rev.*, 120, 947–957, https:// doi.org/10.1175/1520-0493(1992)120<0947:TCECOH>2.0.CO;2.
- Cai, Q., and X. Tang, 2019: Effect of the eyewall cold pool on the inner rainband of a tropical cyclone. *J. Geophys. Res. Atmos.*, 124, 1292–1306, https://doi.org/10.1029/2018JD029107.
- Chen, G., 2018: Secondary eyewall formation and concentric eyewall replacement in association with increased low-level innercore diabatic cooling. *J. Atmos. Sci.*, 75, 2659–2685, https:// doi.org/10.1175/JAS-D-17-0207.1.
- —, C. C. Wu, and Y. H. Huang, 2018: The role of near-core convective and stratiform heating/cooling in tropical cyclone structure and intensity. *J. Atmos. Sci.*, 75, 297–326, https://doi.org/10.1175/JAS-D-17-0122.1.
- Corbosiero, K. L., and J. Molinari, 2002: The effects of vertical wind shear on the distribution of convection in tropical cyclones. *Mon. Wea. Rev.*, 130, 2110–2123, https://doi.org/10.1175/ 1520-0493(2002)130<2110:TEOVWS>2.0.CO;2.
- —, and —, 2003: The relationship between storm motion, vertical wind shear, and convective asymmetries in tropical cyclones. *J. Atmos. Sci.*, 60, 366–376, https://doi.org/10.1175/1520-0469(2003)060<0366:TRBSMV>2.0.CO;2.
- Dai, Y., S. J. Majumdar, and D. S. Nolan, 2017: Secondary eyewall formation in tropical cyclones by outflow-jet interaction. *J. Atmos. Sci.*, 74, 1941–1958, https://doi.org/10.1175/JAS-D-16-0322.1.
- Davis, C., C. Snyder, and A. C. Didlake Jr., 2008: A vortex-based perspective of eastern Pacific tropical cyclone formation. *Mon. Wea. Rev.*, 136, 2461–2477, https://doi.org/10.1175/ 2007MWR2317.1.
- Didlake, A. C., and R. A. Houze Jr., 2013: Dynamics of the stratiform sector of a tropical cyclone rainband. *J. Atmos. Sci.*, **70**, 1891–1911, https://doi.org/10.1175/JAS-D-12-0245.1.
- ——, P. D. Reasor, R. F. Rogers, and W. C. Lee, 2018: Dynamics of the transition from spiral rainbands to a secondary eyewall in Hurricane Earl (2010). J. Atmos. Sci., 75, 2909–2929, https:// doi.org/10.1175/JAS-D-17-0348.1.

- Fang, J., and F. Zhang, 2012: Effect of beta shear on simulated tropical cyclones. Mon. Wea. Rev., 140, 3327–3346, https:// doi.org/10.1175/MWR-D-10-05021.1.
- Gamache, J. F., F. D. Marks, and F. Roux, 1995: Comparison of three airborne Doppler sampling techniques with airborne in situ wind observations in Hurricane Gustav (1990). *J. Atmos. Oceanic Technol.*, **12**, 171–181, https://doi.org/10.1175/1520-0426(1995)012<0171:COTADS>2.0.CO;2.
- Grell, G. A., and S. R. Freitas, 2014: A scale and aerosol aware stochastic convective parameterization for weather and air quality modeling. *Atmos. Chem. Phys.*, 14, 5233–5250, https:// doi.org/10.5194/acp-14-5233-2014.
- Hawkins, J. D., M. Helveston, T. F. Lee, F. J. Turk, K. Richardson, C. Sampson, J. Kent, and R. Wade, 2006: Tropical cyclone multiple eyewall configurations. 27th Conf. on Hurricanes and Tropical Meteorology, Monterey, CA, Amer. Meteor. Soc., 6B.1, https://doi.org/10.1017/CBO9781107415324.004.
- Hence, D. A., and R. A. Houze, 2012: Vertical structure of tropical cyclones with concentric eyewalls as seen by the TRMM Precipitation Radar. J. Atmos. Sci., 69, 1021–1036, https://doi.org/ 10.1175/JAS-D-11-0119.1.
- Hong, S. Y., J. Dudhia, and S. H. Chen, 2004: A revised approach to ice microphysical processes for the bulk parameterization of clouds and precipitation. *Mon. Wea. Rev.*, 132, 103–120, https://doi.org/10.1175/1520-0493(2004)132<0103: ARATIM>2.0.CO;2.
- Huang, Y. H., M. T. Montgomery, and C. C. Wu, 2012: Concentric eyewall formation in Typhoon Sinlaku (2008). Part II: Axisymmetric dynamical processes. *J. Atmos. Sci.*, 69, 662– 674, https://doi.org/10.1175/JAS-D-11-0114.1.
- Judt, F., and S. S. Chen, 2010: Convectively generated potential vorticity in rainbands and formation of the secondary eyewall in Hurricane Rita of 2005. J. Atmos. Sci., 67, 3581–3599, https://doi.org/10.1175/2010JAS3471.1.
- Kepert, J. D., 2013: How does the boundary layer contribute to eyewall replacement cycles in axisymmetric tropical cyclones? *J. Atmos. Sci.*, 70, 2808–2830, https://doi.org/10.1175/JAS-D-13-046.1.
- —, and Y. Wang, 2001: The dynamics of boundary layer jets within the tropical cyclone core. Part II: Nonlinear enhancement. *J. Atmos. Sci.*, **58**, 2485–2501, https://doi.org/10.1175/1520-0469(2001)058<2485:TDOBLJ>2.0.CO;2.
- Kossin, J. P., and M. Sitkowski, 2009: An objective model for identifying secondary eyewall formation in hurricanes. *Mon. Wea. Rev.*, 137, 876–892, https://doi.org/10.1175/2008MWR2701.1.
- Kuo, H. C., C. P. Chang, Y. T. Yang, and H. J. Jiang, 2009: Western North Pacific typhoons with concentric eyewalls. *Mon. Wea. Rev.*, 137, 3758–3770, https://doi.org/10.1175/2009MWR2850.1.
- Li, Q., Y. Wang, and Y. Duan, 2014: Effects of diabatic heating and cooling in the rapid filamentation zone on structure and intensity of a simulated tropical cyclone. *J. Atmos. Sci.*, **71**, 3144–3163, https://doi.org/10.1175/JAS-D-13-0312.1.
- Martinez, J., M. M. Bell, R. F. Rogers, and J. D. Doyle, 2019: Axisymmetric potential vorticity evolution of Hurricane Patricia (2015). J. Atmos. Sci., 76, 2043–2063, https://doi.org/ 10.1175/JAS-D-18-0373.1.
- Montgomery, M. T., and R. J. Kallenbach, 1997: A theory for vortex Rossby-waves and its application to spiral bands and intensity changes in hurricanes. *Quart. J. Roy. Meteor. Soc.*, 123, 435–465, https://doi.org/10.1002/qj.49712353810.
- Moon, Y., and D. S. Nolan, 2010: Dynamic response of the hurricane wind field to spiral rainband heating. *J. Atmos. Sci.*, **67**, 1779–1805, https://doi.org/10.1175/2010JAS3171.1.

- Munsell, E. B., and F. Zhang, 2014: Prediction and uncertainty of Hurricane Sandy (2012) explored through a real-time cloud-permitting ensemble analysis and forecast system assimilating airborne Doppler radar observations. *J. Adv. Model. Earth Syst.*, **6**, 38–58, https://doi.org/10.1002/2013MS000297.
- Noh, Y., W. G. Cheon, S. Y. Hong, and S. Raasch, 2003: Improvement of the K-profile model for the planetary boundary layer based on large eddy simulation data. *Bound.-Layer Meteor.*, 107, 401–427, https://doi.org/10.1023/A:1022146015946.
- Nystrom, R. G., and F. Zhang, 2019: Practical uncertainties in the limited predictability of the record-breaking intensification of Hurricane Patricia (2015). Mon. Wea. Rev., 147, 3535–3556, https://doi.org/10.1175/MWR-D-18-0450.1.
- —, E. B. Munsell, S. A. Braun, J. A. Sippel, Y. Weng, and K. Emanuel, 2018: Predictability and dynamics of Hurricane Joaquin (2015) explored through convection-permitting ensemble sensitivity experiments. J. Atmos. Sci., 75, 401–424, https://doi.org/10.1175/JAS-D-17-0137.1.
- Qiu, X., and Z. M. Tan, 2013: The roles of asymmetric inflow forcing induced by outer rainbands in tropical cyclone secondary eyewall formation. J. Atmos. Sci., 70, 953–974, https:// doi.org/10.1175/JAS-D-12-084.1.
- ——, and Q. Xiao, 2010: The roles of vortex Rossby waves in hurricane secondary eyewall formation. *Mon. Wea. Rev.*, **138**, 2092–2109, https://doi.org/10.1175/2010MWR3161.1.
- Riemer, M., 2016: Meso-β-scale environment for the stationary band complex of vertically sheared tropical cyclones. Quart. J. Roy. Meteor. Soc., 142, 2442–2451, https://doi.org/10.1002/gi.2837.
- Rozoff, C. M., W. H. Schubert, B. D. McNoldy, and J. P. Kossin, 2006: Rapid filamentation zones in intense tropical cyclones. J. Atmos. Sci., 63, 325–340, https://doi.org/10.1175/JAS3595.1.
- ——, D. S. Nolan, J. P. Kossin, F. Zhang, and J. Fang, 2012: The roles of an expanding wind field and inertial stability in tropical cyclone secondary eyewall formation. *J. Atmos. Sci.*, 69, 2621–2643, https://doi.org/10.1175/JAS-D-11-0326.1.
- Sitkowski, M., J. P. Kossin, and C. M. Rozoff, 2011: Intensity and structure changes during hurricane eyewall replacement cycles. *Mon. Wea. Rev.*, 139, 3829–3847, https://doi.org/10.1175/ MWR-D-11-00034.1.
- —, —, and J. A. Knaff, 2012: Hurricane eyewall replacement cycle thermodynamics and the relict inner eyewall circulation. *Mon. Wea. Rev.*, **140**, 4035–4045, https://doi.org/10.1175/MWR-D-11-00349.1.
- Skamarock, W. C., and Coauthors, 2008: A description of the Advanced Research WRF version 3. NCAR Tech. Note NCAR/TN-475+STR, 113 pp., https://doi.org/10.5065/D68S4MVH.
- Stewart, S. R., 2017: Hurricane Matthew. National Hurricane Center Rep., 96 pp., https://doi.org/AL142016.
- Sun, Y. Q., Y. Jiang, B. Tan, and F. Zhang, 2013: The governing dynamics of the secondary eyewall formation of Typhoon Sinlaku (2008). J. Atmos. Sci., 70, 3818–3837, https://doi.org/ 10.1175/JAS-D-13-044.1.
- Tang, X., Z. Tan, J. Fang, Y. Q. Sun, and F. Zhang, 2017: Impacts of the diurnal radiation cycle on secondary eyewall formation. *J. Atmos. Sci.*, 74, 3079–3098, https://doi.org/10.1175/JAS-D-17-0020.1.
- Terwey, W. D., and M. T. Montgomery, 2008: Secondary eyewall formation in two idealized, full-physics modeled hurricanes. J. Geophys. Res., 113, D12112, https://doi.org/10.1029/ 2007JD008897.
- Tyner, B., P. Zhu, J. A. Zhang, S. Gopalakrishnan, F. Marks, and V. Tallapragada, 2018: A top-down pathway to secondary eyewall formation in simulated tropical cyclones. *J. Geophys. Res. Atmos.*, 123, 174–197, https://doi.org/10.1002/2017JD027410.

- Vetterling, W. T., S. A. Teukolsky, W. H. Press, and B. P. Flannery, 1992: *Numerical Recipes in Fortran 77: The Art of Scientific Computing*. Cambridge University Press, 1010 pp.
- Wang, H., C. C. Wu, and Y. Wang, 2016: Secondary eyewall formation in an idealized tropical cyclone simulation: Balanced and unbalanced dynamics. J. Atmos. Sci., 73, 3911–3930, https://doi.org/10.1175/JAS-D-15-0146.1.
- —, Y. Wang, J. Xu, and Y. Duan, 2019: The axisymmetric and asymmetric aspects of the secondary eyewall formation in a numerically simulated tropical cyclone under idealized conditions on an f plane. J. Atmos. Sci., 76, 357–378, https://doi.org/10.1175/JAS-D-18-0130.1.
- Wang, Y., 2009: How do outer spiral rainbands affect tropical cyclone structure and intensity? *J. Atmos. Sci.*, 66, 1250–1273, https://doi.org/10.1175/2008JAS2737.1.
- Weng, Y., and F. Zhang, 2012: Assimilating airborne Doppler radar observations with an ensemble Kalman filter for convection-permitting hurricane initialization and prediction: Katrina (2005). Mon. Wea. Rev., 140, 841–859, https://doi.org/ 10.1175/2011MWR3602.1.
- —, and —, 2016: Advances in convection-permitting tropical cyclone analysis and prediction through EnKF assimilation of reconnaissance aircraft observations. *J. Meteor. Soc. Japan*, **94**, 345–358, https://doi.org/10.2151/jmsj.2016-018.
- Willoughby, H. E., J. A. Clos, and M. G. Shoeibah, 1982: Concentric eye walls, secondary wind maxima, and the evolution of hurricane vortex. J. Atmos. Sci., 39, 395–411, https://doi.org/10.1175/1520-0469(1982)039<0395:CEWSWM> 2.0 CO:2.
- ——, F. D. Marks, and R. H. Feinberg, 1984: Stationary and moving convective bands in hurricanes. *J. Atmos. Sci.*, 41, 3189–3211, https://doi.org/10.1175/1520-0469(1984)041<3189: SAMCBI>2.0.CO;2.
- Wu, C.-C., Y.-H. Huang, and G.-Y. Lien, 2012: Concentric eyewall formation in Typhoon Sinlaku (2008). Part I: Assimilation of T-PARC data based on the ensemble Kalman filter (EnKF). *Mon. Wea. Rev.*, 140, 506–527, https://doi.org/10.1175/MWR-D-11-00057.1.
- Wunsch, K. E. D., and A. C. Didlake, 2018: Analyzing tropical cyclone structures during secondary eyewall formation using aircraft in situ observations. *Mon. Wea. Rev.*, 146, 3977–3993, https://doi.org/10.1175/MWR-D-18-0197.1.
- Yu, C.-L., and A. C. Didlake, 2019: Impact of stratiform rainband heating on the tropical cyclone wind field in idealized simulations. J. Atmos. Sci., 76, 2443–2462, https://doi.org/10.1175/ JAS-D-18-0335.1.
- Zhang, F., and Y. Weng, 2015: Predicting hurricane intensity and associated hazards: A five-year real-time forecast experiment with assimilation of airborne Doppler radar observations. *Bull. Amer. Meteor. Soc.*, 96, 25–33, https://doi.org/10.1175/ BAMS-D-13-00231.1.
- —, D. Tao, Y. Q. Sun, and J. D. Kepert, 2017: Dynamics and predictability of secondary eyewall formation in sheared tropical cyclones. *J. Adv. Model. Earth Syst.*, 9, 89–112, https://doi.org/10.1002/2016MS000729.
- Zhu, P., and Coauthors, 2015: Impact of subgrid-scale processes on eyewall replacement cycle of tropical cyclones in HWRF system. *Geophys. Res. Lett.*, 42, 10 027–10 036, https://doi.org/ 10.1002/2015GL066436.
- Zhu, Z., and P. Zhu, 2014: The role of outer rainband convection in governing the eyewall replacement cycle in numerical simulations of tropical cyclones. *J. Geophys. Res. Atmos.*, 119, 8049–8072, https://doi.org/10.1002/2014JD021899.